Modélisation des fluctuations du fond infrarouge

Sommaire

7.1 Présentation

Le fond infrarouge n'est pas constant sur tout le ciel. En effet, bien que l'Univers soit homogène et isotrope, le nombre de galaxies infrarouges sur une ligne de visée varie à cause des fluctuations statistiques. Elles sont poissoniennes aux petites échelles, mais il existe également des fluctuations structurées aux grandes échelles suivant les grandes structures de l'Univers. Etudier les fluctuations du fond infrarouge fournit donc des informations sur la manière dont les galaxies infrarouges peuplent les halos de matière noire.

L'outil statistique le plus adapté pour étudier ces fluctuations est le spectre de puissance, $P(\vec{k})$, qui est le carré du module de la transformée de Fourier du signal étudié. L'Univers étant statistiquement isotrope[1], le spectre de puissance ne dépend donc pas de la direction de $\vec{k}$, mais juste de sa norme. On étudie donc en général la fonction à une dimension $P(|\vec{k}|)$, noté souvent simplement $P(k)$. Lorsqu'on étudie les grandes échelles, on ne peut plus considérer le ciel comme un plan. Dans ce cas, on utilise une décomposition sur la base des harmoniques sphériques à la place de celle de Fourier. L'équivalent du P(k) dans cette base est noté C_l. Aux petites échelles, on a $P(k) = C_l$ pour $l = 2\pi k$. Ces deux conventions sont utilisées pour étudier les fluctuations du CIB.

7.2 Fluctuations non-corrélées

7.2.1 Niveau des fluctuations poissoniennes

Le niveau des fluctuations non-corrélées (ou poissoniennes) du fond infrarouge peut se calculer facilement à partir des comptages de sources. On considère un intervalle de flux $[S_k, S_k + \Delta S_k]$. Le nombre de sources par unité d'angle solide n_k comprises dans cet intervalle est

$$n_k = \frac{dN}{dS}\Delta S_k. \tag{7.1}$$

Dans le cas poissonien, la variance sur nombre de sources dans cet intervalle est donc

$$\sigma^2_{B_k} = n_k \times S_k^2. \tag{7.2}$$

La contribution B_k de ces sources au fond vaut, quant à elle,

$$B_k = n_k \times S_k. \tag{7.3}$$

On en déduit la variance σ^2_B sur la contribution totale au fond ($B = \sum_k B_k$)

$$\sigma^2_B = \sum_k n_k S_k^2 = \frac{dN}{dS} S_k^2 \Delta S_k. \tag{7.4}$$

On peut alors passer à la limite intgrale :

$$\sigma^2_B = \int_0^{S_c} \frac{dN}{dS} S^2 dS, \tag{7.5}$$

où S_c est le flux de coupure du nettoyage des sources brillantes. Ce nettoyage est nécessaire car l'intégrale ne converge pas en $+\infty$ dans le cas euclidien ($dN/dS \propto S^{-2.5}$). En

[1]En pratique, à cause des grandes structures, il existe des surdensités dans l'Univers. Néanmoins, ces surdensités sont des fluctuations statistiques : tous les points ont la même distribution de probabilité *a priori*.

λ μm	Référence	S_{cut} mJy	$P_{SN,mes}$ Jy^2.sr^{-1}	$P_{SN,model}$ Jy^2.sr^{-1}	$<z_{mod}>$
60	Miville-Deschênes *et al.* (2002)	1000	1600±300	2089±386	0.20±0.01
100	Miville-Deschênes *et al.* (2002)	700	5800±1000	7364±1232	0.38±0.03
160	Lagache *et al.* (2007)	200	9848±120	10834±3124	0.73±0.06
250	Viero *et al.* (2009)	500	11400±1000	11585±2079	0.81±0.08
250	Amblard et Hermes (2010)	50	6100±120	6726±1207	1.09±0.06
350	Viero *et al.* (2009)	400	6300±500	5048±1083	1.17±0.12
350	Amblard et Hermes (2010)	50	4600±70	4446±1320	1.32±0.11
500	Viero *et al.* (2009)	-	2700±200	1677±484	1.59±0.21
500	Amblard et Hermes (2010)	50	1800±80	1369±537	1.85±0.21
1363	Hall *et al.* (2010)	15	17±2	10±3	4.07±0.24

TABLE 7.1 – Niveau des fluctuations non corrélées du fond infrarouge et comparaison des mesures avec les prédictions du modèle de Béthermin *et al.* (2011). Les incertitudes sur les prédictions prennent en compte la calibration. Le *redshift* moyen $<z_{model}>$ des fluctuations est celui prédit par le modèle. Extrait de Béthermin *et al.* (2011).

général, cette coupure est placée relativement basse (proche de la limite de complétude à 95%) pour fournir une meilleure contrainte sur les sources faibles.

Nous avons comparé les prédictions du modèle de Béthermin *et al.* (2011) (voir Chap. 6) avec les mesures des fluctuations poissoniennes. Il y a un très bon accord en dessous de $\lambda < 500\mu$m (Miville-Deschênes *et al.* (2002); Lagache *et al.* (2007); Viero *et al.* (2009); Amblard et Hermes (2010)). Le modèle a tendance à légèrement sous-estimer (environ 30%) les fluctuations à plus grande longueur d'onde (Viero *et al.* (2009); Amblard et Hermes (2010); Hall *et al.* (2010)). On remarque également que les fluctuations à grande longueur d'onde sont dominées par les hauts *redshifts*. Les fluctuations dans le domaine millimétrique fournissent donc des contraintes très importantes sur les galaxies infrarouges à z>4.

7.2.2 Niveau des fluctuations poissoniennes des spectres croisés

On peut de la même manière calculer le niveau poissonien (aux petites échelles) du spectre de puissance croisé entre deux bandes. On considère deux bandes A et B. Le nombre de sources n_{kl} dans une tranche de flux $[S_k, S_k + \Delta S_k]$ et de redshift $[z_l, z_l + \Delta z_l]$ est :

$$n_{kl} = \frac{dN}{dS\,dz}\Delta S_k \Delta z_l \tag{7.6}$$

Si on ne considère qu'une seule population de galaxies et une tranche de flux et *redshift* assez fine, la covariance entre les deux bandes $\sigma_{AB,kl}$ est

$$\sigma_{AB,kl} = n_{kl} S_{A,kl} S_{B,kl} = n_{kl} S^2_{A,kl} C_{BA,kl}, \tag{7.7}$$

où $C_{BA,kl}$ est la couleur entre la bande B et la bande A pour une population dans l'intervalle considéré. Si on somme sur les deux populations et sur tous les intervalles, on obtient alors

$$\sigma_{AB} = \sum_{pop} \sum_{k} \sum_{l} n_{pop,kl} S^2_{A,kl} C_{BA,pop,kl}, \tag{7.8}$$

où $n_{pops,kl}$ est le nombre de sources dans l'intervalle considéré appartenant à la population considérée, et $C_{BA,pop,kl}$ la couleur d'une source appartenant l'intervalle et la population sélectionnés. On peut alors passer à la limite intégrale pour obtenir :

$$\sigma_{AB} = \sum_{pop} \int_{S_A=0}^{\infty} \int_{z=0}^{\infty} H(S_A < S_{A,c}, C_{BA,pop} S_A < S_{B,c}) \frac{dN_{pop}}{dS\, dz} S^2_A C_{BA,pop} dS_A dz, \tag{7.9}$$

où $H(P_1, P_2)$ vaut 1 lorsque P_1 et P_2 sont vraies, et 0 sinon. $S_{A,c}$ et $S_{B,c}$ sont les coupures en flux dans les bandes A et B. On peut également montrer que :

$$\sigma_{AB} = \int_{S_A=0}^{S_{A,c}} \int_{S_B=0}^{S_{B,c}} \frac{dN_{pop}}{dS_A dS_B} S_A S_B dS_A dS_B \tag{7.10}$$

Néanmoins, cette formule est moins pratique à utiliser ($dN/dS_A/dS_B$ n'est pas trivial à calculer contrairement $dN_{pop}/dS_A/dz$).

Le spectre de puissance croisé entre les cartes BLAST et ACT a été mesuré par Hajian *et al.* (2011). J'ai fourni grâce à mon modèle une prédiction des fluctuations poissoniennes croisées afin de les comparer aux observations. Le modèle est en relativement bon accord avec les niveaux poissoniens prédits (voire Fig. 7.1).

7.2.3 Fluctuations poissoniennes de la polarisation ?

La lumière émise par une galaxie infrarouge n'a aucune raison de ne pas être polarisée. La polarisation du fond infrarouge pourrait donc présenter des propriétés particulières. Elles peuvent être estimées par un modèle simple.

On note I l'intensité totale, I_x l'intensité polarisée selon x, et I_y l'intensité polarisée selon y. On introduit également Q = I_x-I_y et U = I^{45}_x - I^{45}_y (**?**)), où I^{45}_x (resp. I^{45}_y) est l'intensité selon un axe à 45° avec l'axe x (resp. y). On appelle p la fraction de polarisation donnée par :

$$p = \sqrt{Q^2 + U^2} \times I. \tag{7.11}$$

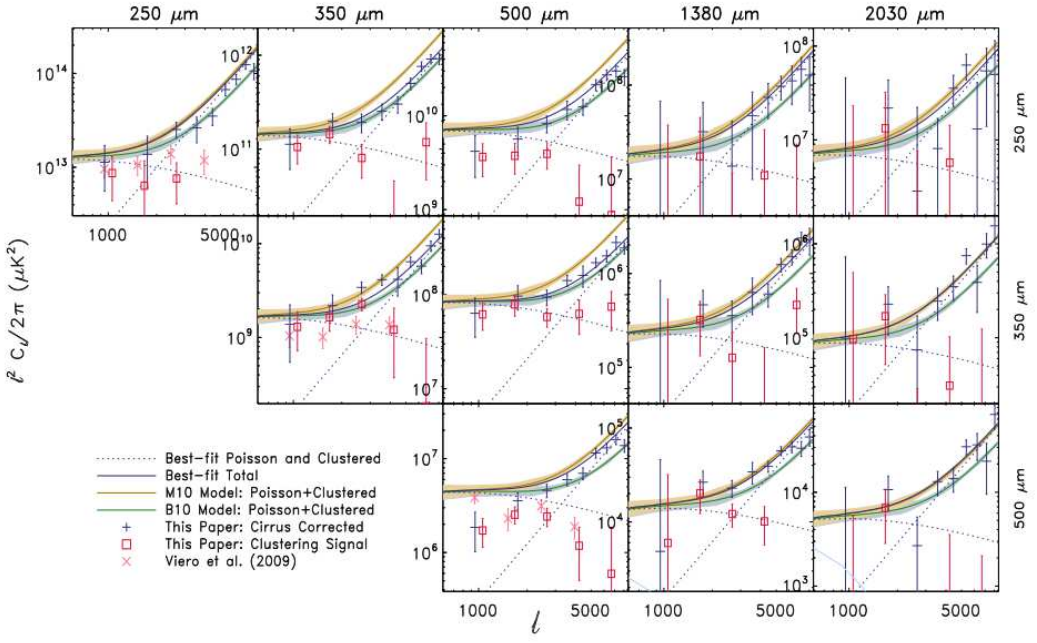

FIGURE 7.1 – Spectres de puissance croisés observés par BLAST et ACT (croix bleues). Le modèle de Béthermin *et al.* (2011) est en vert et celui de Marsden *et al.* (2010) est en doré. Extrait de Hajian *et al.* (2011).

Pour un objet dont la fraction de polarisation est p, les valeurs de Q et U sont :

$$Q = pIcos(2\alpha) \quad (7.12)$$
$$U = pIsin(2\alpha), \quad (7.13)$$

où α indique l'angle de polarisation. On supposera dans ce modèle que α est aléatoire (entre 0 et π), de densité de probabilité constante et indépendant d'une source à l'autre.

On peut montrer facilement que la polarisation moyenne du fond est nulle. On considère un intervalle de flux $[S_i, S_i + \Delta S_i]$ et d'angle de polarisation $[\alpha_j, \alpha_j + \Delta\alpha_j]$. Le contribution de cet intervalle à Q est

$$Q_{ij} = pS_i cos(2\alpha_j)\frac{dN}{dS_i}\frac{\Delta\alpha_j}{\pi}\Delta S_i \quad (7.14)$$

Si on somme sur tous les intervalles et qu'on passe à la limite intégrale, on obtient :

$$Q = \int_0^{S_c} pS\frac{dN}{dS_i}dS \times \int_0^{\pi} cos(2\alpha)\frac{d\alpha}{\pi} = 0 \quad (7.15)$$

Les galaxies n'ayant aucune raisons d'être alignées, le fond infrarouge a donc bien une polarisation à moyenne nulle.

En revanche, il peut exister des fluctuations statistiques en polarisation. En effet, dans l'hypothèse poissonienne, la variance sur le nombre de sources dans un intervalle de flux et d'angle de polarisation est

$$\sigma^2_{n,ij} = \frac{\Delta\alpha_j}{\pi}\frac{dN}{dS_i}\Delta S_i. \quad (7.16)$$

La variance sur la contribution à Q des sources dans cet intervalle est donc

$$\sigma^2_{Q,ij} = \frac{\Delta\alpha_j}{\pi}\frac{dN}{dS_i}\Delta S_i\left(pS_i cos(2\alpha_j)\right)^2. \quad (7.17)$$

La variance sur Q est alors

$$\sigma^2_{Q,tot} = \sum_i\sum_j \frac{\Delta\alpha_j}{\pi}\frac{dN}{dS_i}\Delta S_i\left(pS_i cos(2\alpha_j)\right)^2. \quad (7.18)$$

On peut passer à la limite intégrale :

$$\sigma^2_{Q,tot} = \int_{\alpha=0}^{\pi}\int_{S=0}^{S_c} p^2S^2cos^2(\alpha)\frac{dN}{dS}dS\,d\alpha \quad (7.19)$$
$$= \frac{p^2}{2}\int_{S=0}^{S_c} S^2\frac{dN}{dS}dS = \frac{p^2}{2}\sigma^2_{I,tot}, \quad (7.20)$$

où $\sigma^2_{I,tot}$ est le niveau des fluctuations poissoniennes en intensité. Les fluctuations en polarisation ont donc $p^2/2$ fois plus faibles que les fluctuation en intensité. Si on suppose que p est de l'ordre de 1%, il y a donc plus de quatre ordres de grandeur entre les fluctuations en intensité et en polarisation. Ces dernières semblent donc être un phénomène indétectable aujourd'hui. Le satellite *Planck* devrait mesurer prochainement la polarisation de galaxies locales, permettant à l'avenir de mieux contraindre p et donc l'estimation du niveau de ces fluctuations polarisées.

7.3 Fluctuations corrélées

7.3.1 Modélisation

Le modèle présenté ici est publié dans Planck Collaboration *et al.* (2011) et Pénin *et al.* (2011a).

D'après Haiman et Knox (2000) et Knox *et al.* (2001), et dans le cadre de l'approximation de Limber (ciel plat), le spectre de puissance des fluctuations corrélées du fond infrarouge se calcule de la manière suivante :

$$C_l^{\lambda\lambda'} = \int \left(\frac{dD_c}{dz}\right)\left(\frac{1}{(1+z)D_c}\right)^2 \bar{j}_\nu(z)\bar{j}_{\nu'}(z)P_{gg}(k = l/\chi, z)dz, \tag{7.21}$$

où $C_l^{\lambda\lambda'}$ est le spectre de puissance croisé entre les longueurs d'onde λ et λ', D_c la distance comobile correspondant au *redshift* z, $P_{gg}(k = l/\chi, z)$ est le spectre de puissance des galaxies à un *redshift* z[2], et $\bar{j}_\nu(z)$ est l'émissivité moyenne des galaxies par unité de volume comobile. Les fluctuations corrélées dépendent donc de trois ingrédients : la cosmologie, la distribution spatiale des galaxies, et l'évolution des émissivités.

L'émissivité $\bar{j}_\nu(z)$ provient du modèle d'évolution des galaxies présenté Chap. 6 et se calcule de la manière suivante :

$$\bar{j}_\nu(z) = \frac{(1+z)}{dDc/dz}\int_0^{S_{cut}} S\,\frac{d^2N}{dS\,dz}dS. \tag{7.22}$$

Le partie corrélée du spectre de puissance du fond infrarouge dépend donc, comme sa partie poissonienne, de l'évolution des galaxies. En revanche, seule la partie corrélée est affectée par la distribution spatiale des objets.

[2]On suppose ici implicitement que les galaxies lumineuses et peu lumineuses ont la même distribution spatiale.

La manière la plus simple d'estimer le spectre de puissance des galaxies est de supposer une relation de proportionnalité avec celui de la matière noire :

$$P_{gg}(k,z) = b_{lin}^2 P_{lin}(k,z) \tag{7.23}$$

où b_{lin} est un paramètre appelé le biais linéaire, et $P_{lin}(k,z)$ est le spectre de puissance de la matière noire calculé à partir de la théorie des perturbations linéaires. Ce modèle sera donc surtout valable aux grandes échelles.

Il est toutefois possible de décrire plus finement la distribution spatiale des galaxies grâce à un modèle de halo (Cooray et Sheth (2002)). Dans ce type de modèle, le spectre de puissance des galaxies est alors la somme de deux termes : un premier dû aux corrélations à l'intérieur d'un halo P_{1h}, et un second dû aux corrélations entre les galaxies de deux halos différents P_{2h}. Le terme 1-halo dépend du nombre de galaxies dans les halos, ainsi que du profil de densité, ces deux quantités dépendant de la masse du halo, M :

$$P_{1h}(k) = \int \frac{dN}{dM} \frac{\left\langle N_{gal}(N_{gal}-1)\right\rangle}{\bar{n}_{gal}^2} u^2(k,M) dM, \tag{7.24}$$

où dN/dM est la fonction de masse des halos, N_{gal} est le nombre de galaxies, $\bar{n}_{gal}$ la densité moyenne de galaxies, et $u(k,M)$ est la transformée de Fourier normalisée du profil de densité d'un halo de masse M. On peut, par exemple, pendre un profil NFW (Navarro *et al.* (1997)). Le nombre de galaxies dans un halo, N_{gal}, peut quant à lui être décrit par un modèle du type de celui de Zheng *et al.* (2005) :

$$\left\langle N_{gal}\right\rangle = \langle N_{cen}\rangle + \left\langle N_{gal}\right\rangle. \tag{7.25}$$

N_{cen} est le nombre moyen de galaxie central dans un halo donné par :

$$\langle N_{cen}\rangle = \frac{1}{2}\left(1 + erf\left(\frac{log(M) - log(M_{min})}{\sigma_{log(M)}}\right)\right), \tag{7.26}$$

avec M_{min} la masse minimale typique d'un halo pour qu'il puisse contenir une galaxie centrale et $\sigma_{log(M)}$ décrit la dispersion autour de cette valeur. N_{sat} est le nombre moyen de galaxies satellites donné par :

$$\langle N_{sat}\rangle = \frac{1}{2}\left(1 + erf\left(\frac{log(M) - log(2M_{min})}{\sigma_{log(M)}}\right)\right)\left(\frac{M}{M_{sat}}\right), \tag{7.27}$$

où M_{sat} et α décrivent comment le nombre de satellites augmente avec la masse. Le facteur 2 devant M_{min} est arbitraire et sert à éviter qu'un halo contienne une galaxie satellite et pas de galaxie centrale. La Fig. 7.2 montre comment ces deux quantités évoluent avec la masse du halo hôte.

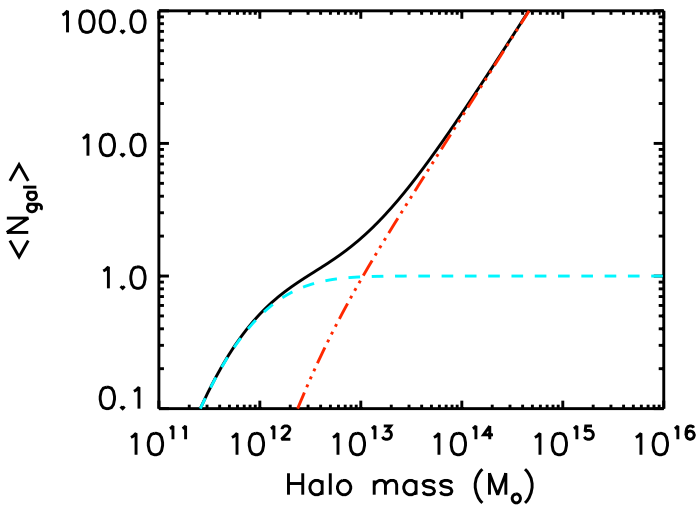

FIGURE 7.2 – Nombre moyen de galaxies dans un halo en fonction de sa masse. *Ligne noire* : nombre total de galaxies. *Tirets cyans* : nombre de galaxies centrales. *Tirets-2-points rouges* : nombre de galaxies satellites. Extrait de Pénin *et al.* (2011a)

Le terme 2-halo est, quant à lui, calculé de la manière suivante :

$$P_{2h} = P_{lin}\left(\int \frac{dN}{dM} b(M) \frac{\langle N_{gal} \rangle}{\bar{n}_{gal}} u(k, M) dM\right)^2 , \tag{7.28}$$

où b(M) est le bias linéaire des halos de masse M. Cette quantité provient d'un ajustement des résultat fournis par les simulations de matière noire (Tinker *et al.* (2010)).

J'ai participé à ce projet de modélisation en fournissant les $\bar{j}_\nu$ issus de mon modèle d'évolution (voir Chap. 6). En effet, les fluctuations corrélées sont très dépendantes du modèle d'évolution sous-jacent, et l'utilisation d'un modèle actualisé était fondamentale. Les Fig. 7.3 et 7.4 comparent les prédictions du modèle de Lagache *et al.* (2004) et de Béthermin *et al.* (2011) pour un même modèle de halos. On constate de forts écarts autour de z=2. L'effet sur le spectre de puissance peut atteindre un facteur 2. De plus, l'utilisation d'un modèle paramétrique permet d'étudier les dégénérescences entre les paramètres d'évolution et de halos (voir Pénin *et al.* (2011a) pour plus de détails).

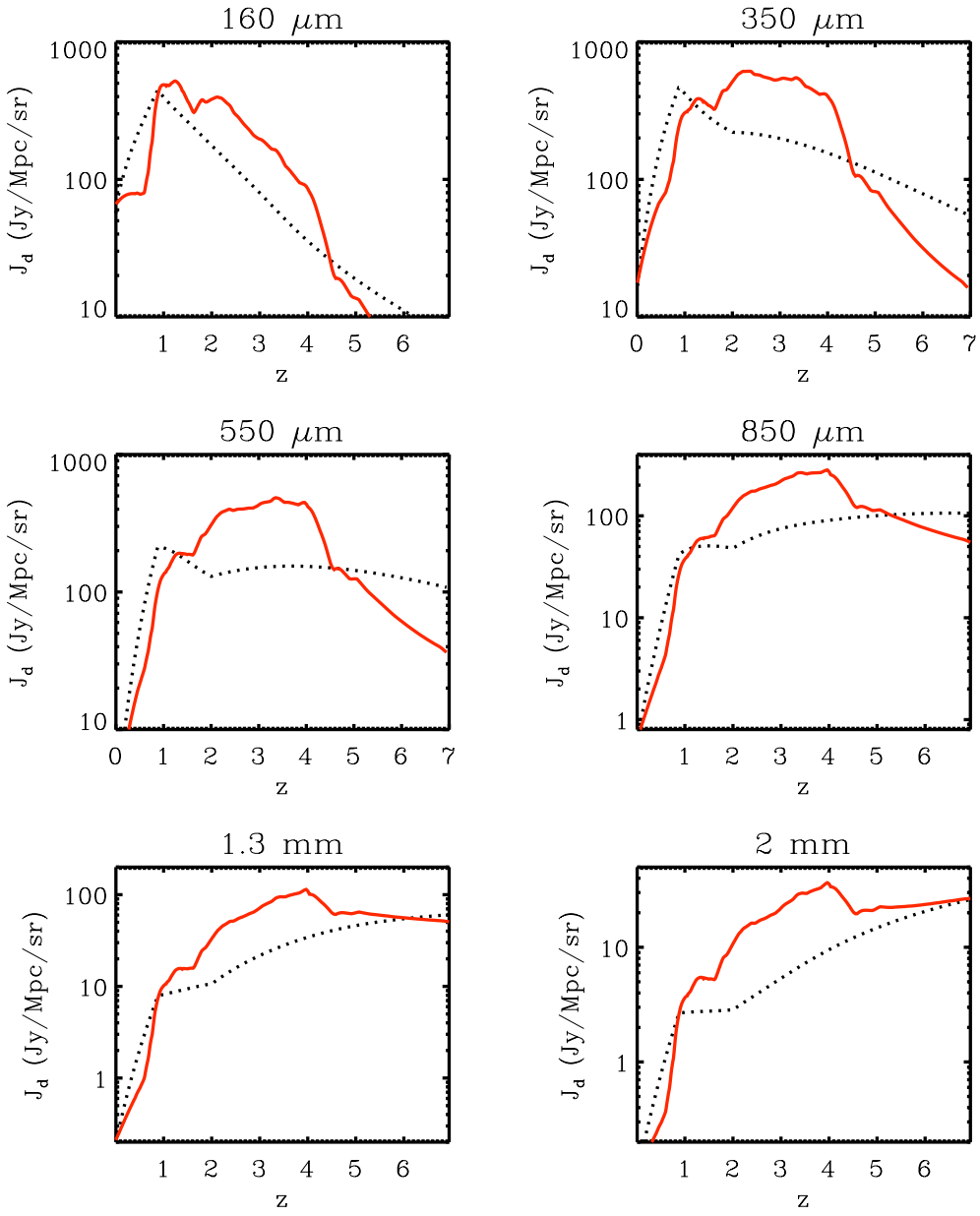

FIGURE 7.3 – Comparaison des émissivités prédites par les modèles de Lagache *et al.* (2004) (en rouge) et de Béthermin *et al.* (2011) (en noir). Extrait de Pénin *et al.* (2011a).

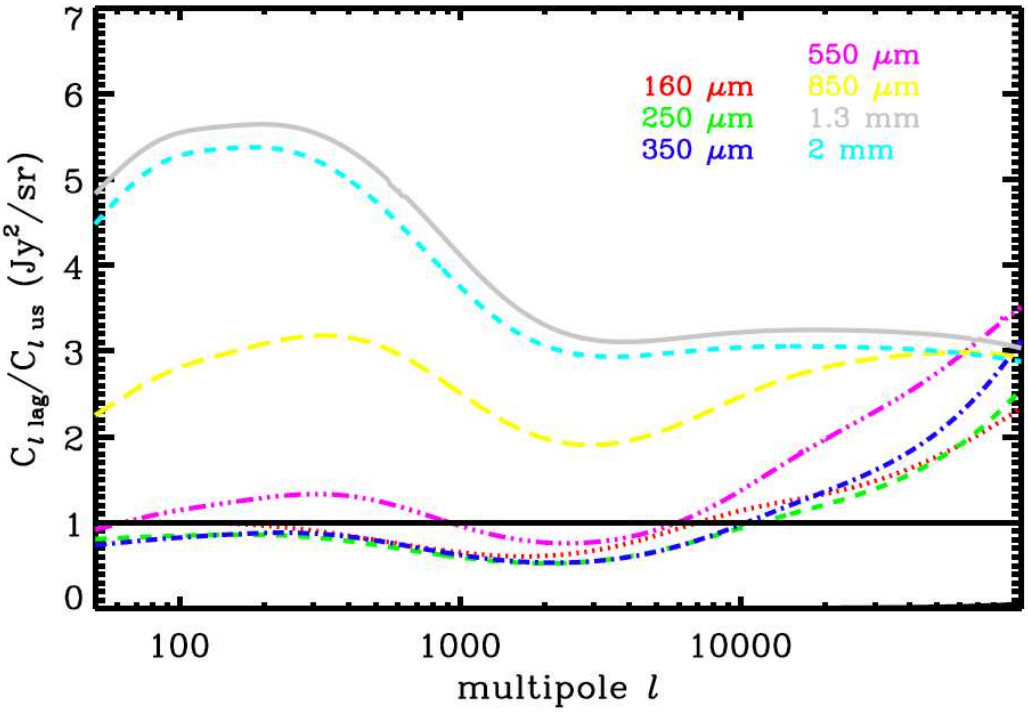

FIGURE 7.4 – Rapport entre les spectres de puissance prédits des fluctuations corrélées par les deux modèles d'évolution. Extrait de Pénin *et al.* (2011a).

7.3.2 Application

Ce modèle a été utilisé par la collaboration *Planck* pour interpréter les fluctuations du fond infrarouge. La Fig. 7.5 représente cette mesure et le meilleur ajustement de ces points. A cause de sa résolution angulaire limitée, *Planck* ne permet pas d'accéder aux petites échelles, et ainsi contraindre le niveau des fluctuations poissoniennes. Nous utilisons donc les niveaux de fluctuations prédites par notre modèle d'évolution. Chaque longueur d'onde est ajustée séparément. En effet, un modèle de halo unique ne parvient pas à reproduire le spectre de puissance observé à toutes les longueurs d'ondes. En revanche, l'ajustement de chaque bande individuellement est très bon. Chaque longueur d'onde est dominée par des *redshifts* différents (voir Chap. 5 et 6). Ceci suggère donc que les propriétés d'occupation des halos évoluent avec le *redshift*. Il est donc nécessaire de développer des modèles plus complexes pour interpréter avec finesse les résultats de *Planck*. Un second ajustement a été réalisé en laissant libre j_ν au-delà de z=3.5. Les dégénérescence sont trop importantes pour faire la moindre conclusion. Ceci montre qu'il n'est pas possible de contraindre à la fois le modèle de halos et l'évolution de l'émissivité avec le seul spectre de puissance. Il est donc important d'utiliser d'autres observables complémentaires pour lever ces dégénérescences.

7.4 Conclusion

Les fluctuations du fond infrarouge contiennent des informations importantes sur les populations faibles. Le niveau poissonien de ces fluctuations ne dépend que de l'évolution des galaxies, et pas de leur distribution spatiale. Ensuite, plus on va à grande longueur d'onde et plus on sonde des populations à grand *redshift*. Ce type de mesure semble par conséquent être une des manières les plus prometteuse de contraindre l'évolution des galaxies infrarouges à z>4. De plus, les fluctuations poissoniennes croisées fournissent des informations complémentaires sur la couleur des sources.

Les fluctuations corrélées, dominant aux plus grandes échelles (au delà de quelques arcmin), fournissent une information dégénérée sur l'évolution et la distribution spatiale des sources infrarouges. L'interprétation semble difficile, mais extrêmement prometteuse. En effet, les fluctuations corrélées dans le domaine millimétrique sondent la structuration spatiale des objets infrarouges à très grand *redshift*. Les fluctuations ont de grandes chances d'être dans la prochaine décennie une des observables phares de l'Univers infrarouge.

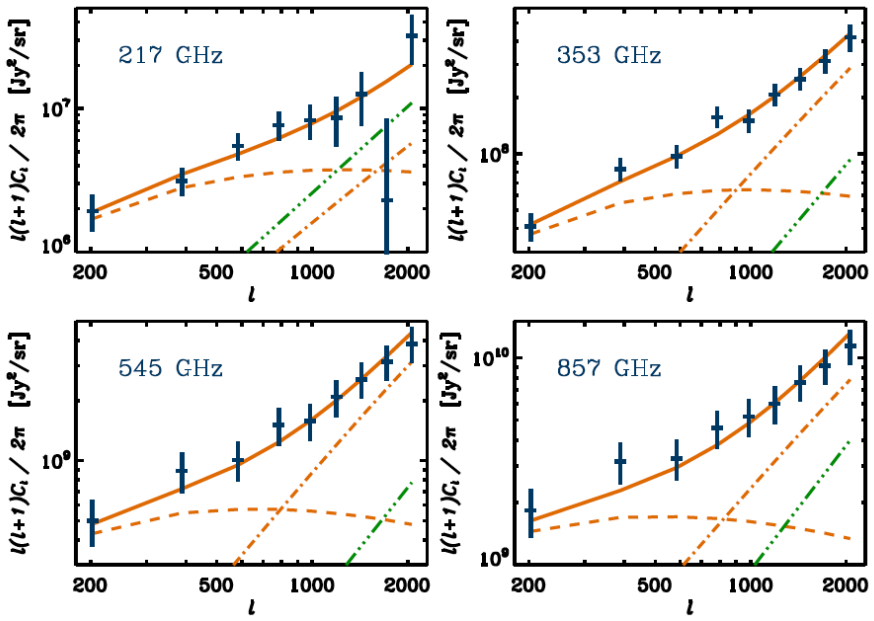

FIGURE 7.5 – Spectre de puissance des fluctuations du fond infrarouge mesuré par le satellite *Planck* (*en bleu*) et son ajustement par notre modèle (*ligne continue jaune*). Les contributions des termes poissonien (*ligne tirets-3 points verte*), 1-halo (*ligne tirets-points jaune*) et 2-halos (*tirets jaune*) sont également représentées. Extrait de Planck Collaboration *et al.* (2011)

7.5 Article : *Modeling the evolution of infrared galaxies : clustering of galaxies in the Cosmic Infrared Background*

Le modèle de fluctuations du fond infrarouge de l'IAS a fait l'objet d'un article soumis à *Astronomy&Astrophysics*.

Astronomy & Astrophysics manuscript no. model˙v3
October 4, 2011

Modeling the evolution of infrared galaxies : clustering of galaxies in the Cosmic Infrared Background

Aurélie Pénin[1,2], Olivier Doré[3,4], Guilaine Lagache[1,2], and Matthieu Béthermin[1,2]

[1] Univ. Paris Sud, Institut d'Astrophysique Spatiale, UMR8617, F-91405 Orsay
[2] CNRS F-91405 Orsay
[3] Jet Propulsion Laboratory, California Institute of Technology, Pasadena, CA 91109
[4] California Institute of Technology, Pasadena, CA 91125

Preprint online version: October 4, 2011

ABSTRACT

Context. Star-forming galaxies are a highly biased tracer of the underlying dark matter density field. Their clustering can be studied through the cosmic infrared background anisotropies. These anisotropies have been measured from 100 μm to 2 mm in the last few years.
Aims. In this paper, we present a fully parametric model allowing a joint analysis of these recent observations.
Methods. In order to develop a coherent model at various wavelengths, we rely on two building blocks. The first one is a parametric model that describes the redshift evolution of the luminosity function of star-forming galaxies. It was introduced in Béthermin et al. (2011) and compares favorably to measured differential number counts and luminosity functions. The second one is a halo model based description of the clustering of galaxies. Starting from a fiducial model, we investigate parameter degeneracies using a Fisher analysis. We then discuss how halo of different mass and redshift, how LIRGs and ULIRGs, contribute to the CIB angular power spectra.
Results. From the Fisher analysis, we conclude that we cannot constrain the parameters of the model of evolution of galaxies using clustering data only. The use of combined data of C_ℓ, counts and luminosity functions improves slightly the constraints but does not remove any degeneracies. On the contrary, the measurement of the anisotropies allows us to set interesting constraints on the halo model parameters, even if some strong degeneracies remain. Using our fiducial model, we establish that the 1-halo and 2-halo terms are not sensitive to the same mass regime. We also illustrate how the 1-halo term can be misinterpreted with the Poisson noise term.
Conclusions. We present a new model of the clustering of infrared galaxies. Our framework allows a coherent and joint analysis of various probes of infrared galaxies : number counts, luminosity functions and clustering measurements. However such a model has a few limitations, as the parameters of the halo occupation suffer from strong degeneracies.

Key words. Infrared : galaxies - Cosmology : large scale structure of the Universe - galaxies :high redshift

1. Introduction

Infrared star-forming galaxies are mainly characterized by a very high star formation rate, tens or even hundreds times larger than that of the Milky Way, ∼10-100 $M_\odot$/year (Kennicutt 1998). The large number of young stars are embedded in dust that absorbs UV starlight and reemits it in the infrared (IR), from 5 μm to 1 mm. As a result, infrared star-forming galaxies emit most of their energy (∼95%) in the IR. In the far IR ($\lambda > 200\mu$m) and sub-millimeter, observations are limited by confusion, small spatial scales are lost because of the poor angular resolution of the instruments. Thus we observe the Cosmic Infrared Background (CIB) (Puget et al. 1996; Fixsen et al. 1998) which is the contribution of infrared star-forming galaxies integrated over the age of the Universe, and its anisotropies. In the near and mid IR a large fraction of the CIB is resolved into sources whereas in the far IR only a few percents is. These fractions can be improved thanks to the use of statistical methods. For instance, at long wavelength, Oliver et al. (2010) directly resolved 15%, 10% and 6% of the CIB at 250, 350 and 500 μm in Herschel/SPIRE data whereas Papovich et al. (2004) resolved 70% of the CIB at 24 μm. Berta et al. (2010) resolved 45% and 52% of the CIB at 100 and 160 μm respectively by integrating number counts in Herschel/PACS data. Stacking 24 μm sources they increased these fractions to 50% and 75% respectively. As a result, sources detected at 24 μm are the main sources of the CIB around its peak at ∼200 μm. The CIB is dominated by objects that get more and more massive as the redshift increases from luminous IR galaxies (LIRGs) with $10^{11}L_\odot < L_{IR} < 10^{12}L_\odot$ at $0.8 < z < 1.2$ with intermediate mass, to extreme LIRGs with $10^{12}L_\odot < L_{IR} < 10^{14}L_\odot$ that dominate at $z > 2$ and with masses $> 10^{11}M_\odot$ (Caputi et al. 2006).
Magliocchetti et al. (2007) and Farrah et al. (2006) derived the two-point correlation function of Ultra LIRGs at $z \simeq 1.6-2.7$ and $1.5 < z < 3$ respectively. They brought to light the very strong clustering of infrared star-forming galaxies and their embedment in very massive halos of $\simeq 10^{13}M_\odot$. Cooray et al. (2010) computed the angular correlation function with Herschel/SPIRE data. They found that 250 μm sources are in DM halos with masses around $10^{12}M_\odot$ that lie at $z \sim 2.1$ whereas bright 500 μm sources are in more massive halos $\simeq 10^{13}M_\odot$ at $z \sim 2.6$. More recently, Magliocchetti et al. (2011) derived the 3D correlation function of infrared sources using Herschel/PACS data up to a redshift of 3. They obtain that their galaxies lie in haloes with $> 10^{12.4}M_\odot$, value that is in agreement with previous studies. However the two-point correlation function is not easily computed using IR data because of confusion. As said before, confusion can be circumvented through the use of statistical

methods. Indeed, clustering can be measured in the correlated CIB anisotropies (CIBA). It has first been detected as an excess of signal at intermediate scales by Lagache et al. (2007) and Grossan & Smoot (2007) at 160 μm in the Spitzer Multiband Imaging Photometer (MIPS) data. These measurements have been followed by the detection in the Balloon-borne Large Aperture Sub-millimeter Telescope (BLAST) data at 250, 350 and 500 μm (Viero et al. 2009) and by that of the South Pole Telescope team (Hall et al. 2010) at 1.3 and 2 mm. More recently Pénin et al. (2011) measured the clustering signal by removing accurately the cirrus contamination at 100 and 160 μm. The power spectrum of the CIBA has also been computed using Herschel/SPIRE at 250, 350 and 500 μm (Amblard et al. 2011), taking advantage of its angular resolution, and using Planck/HFI at 350, 550, 850 μm and 1.3 mm (Planck Collaboration et al. 2011) taking advantage of its sky coverage. Therefore, the clustering of infrared star-forming galaxies in the CIBA has been detected over a large range of wavelengths and angular scales. All these results have been analyzed in several ways, hardly comparable. As a first analysis, Lagache et al. (2007) derived the linear bias, the proportionality coefficient between the fluctuations of the dark matter (DM) density field and emissivities of galaxies. They found $b = 2.4 \pm 0.2$ and Viero et al. (2009) found $b = 3 \pm 0.3$ which implies that these galaxies are a highly biased tracer of DM. The difference between these two biases may be explained by the fact that at longer wavelength, higher redshift infrared star-forming galaxies are probed (Lagache et al. 2005; Fernandez-Conde et al. 2008) and thus are found to be more biased. New measurements needed more complex models. Viero et al. (2009), Amblard et al. (2011) and Planck Collaboration et al. (2011) introduced a halo occupation distribution for the study of CIBA. It describes the DM distribution and especially how galaxies are distributed in one DM halo. It appears that each wavelength must be fitted separately which indicates an evolution of the clustering with the redshift (Planck Collaboration et al. 2011). Most of the models determined the mass of the halos where infrared star-forming galaxies lie and thus where star formation occurs.

In the long term purpose of analysing all these new measurements in a consistent way, we present a new model of the clustering in CIBA. We use the halo model formalism (Cooray & Sheth (2002)) which has been often used in the last few years to predict and to interpret galaxy clustering. We link it to a recent model of infrared star-forming galaxies evolution that reproduces well number counts and luminosity functions (Béthermin et al. 2011). This model of clustering has been successfully used to fit Planck data (Planck Collaboration et al. 2011).

The paper is organized as follows. We describe the model and its parameters in Sect. 2. We set a fiducial model inspired from Viero et al. (2009); Planck Collaboration et al. (2011); Amblard et al. (2011) and compute angular power spectra for several instruments with which we carry out a Fisher analysis in Sect. 4. Sect. 5 is dedicated to interpreting measurements such as the redshift and halo-masses contribution to the power spectrum, the linear bias, the influence of the mean emissivities and the contribution of LIRGs and ULIRGs to power spectra. We finally conclude in Sect. 6. Throughout this study we use the Wilkinson Microwave Anisotropy Probe 7-year Cosmology (Larson et al. 2011).

2. Why a new model?

As said previously several models of clustering in the Cosmic Infrared Background already exist so why constructing a new one? There have been several measurements of the clustering and different models have been applied to analyze each measurement. Moreover their approaches are different which make comparison of the results difficult if not impossible. Thus one single model that ties together all available measurements is appealing, especially to analyze them simultaneously and search for an evolution of the clustering. Such a model requires three ingredients: a DM distribution, a relation between galaxies and DM halos and an evolution of infrared star-forming galaxies.

Lagache et al. (2007), Amblard & Cooray (2007) and Viero et al. (2009) used the model of galaxy evolution of Lagache et al. (2003). This model was the most up to date model at that time. It fitted well differential number counts and luminosity functions measurements from 24 to 850 μm (IRAS, Spitzer/SCUBA). However it does not reproduce very well new measurements, especially differential number counts from Herschel. This is a phenomenological model in which the evolution of the luminosity function was tuned to reproduce the constraints available at that time. It over-predicts the luminosity density at high-z. Moreover, it does not reproduce very well the observed redshift distribution of the CIB (Jauzac et al. 2011). It predicts a peak at $z \sim 1$ that is not observed. The angular power spectra of CIBA strongly depend on the redshift distribution of the sources through the emissivities (see Sect. 3.2). Therefore, a 'valid' distribution in redshift is important and a more robust model in agreement with most recent measurements is needed.

Hall et al. (2010) used the galaxy templates from Lagache et al. (2003) in order to check a simple model with a 'single SED'. This model has only a few parameters that can be changed easily and thus adapted to each of their wavelengths. They fixed the shape of the power spectrum and only changed its amplitude depending on the wavelength. Amblard & Cooray (2007) used the same model of infrared galaxies evolution : they used the luminosity function as a function of redshift at 350 μm coming from Lagache et al. (2003) that they matched to conditional luminosity functions (CLFs). Other wavelengths are extrapolated from the 350 μm. Finally Amblard et al. 2011 avoid using any model of galaxies evolution by letting free the redshift distribution of the cumulative flux coming from the background faint galaxies in several redshift bins.

Concerning the distribution of DM, Viero et al. (2009) and Amblard et al. (2011) used the formalism of the halo model and the same halo occupation number whereas Lagache et al. (2007) and Hall et al. (2010) considered a linear power spectrum for dark matter. Amblard & Cooray (2007) also used the halo model formalism through CLFs. By integrating CLFs on the luminosity, the halo mass function is recovered. However this approach depends on too many parameters that cannot be constrained simultaneously.

In order to construct a new model, we link an up to date model of galaxies evolution to a recent version of the halo model. We use the model of evolution of galaxies of Béthermin et al. (2011). It reproduces well Herschel measurements as well as older ones (from 15 μm to 1.1 mm). It also very well reproduces the redshift distribution of the CIB of Jauzac et al. (2011). We use an updated version of the halo model of Viero et al. (2009), the halo occupation distribution (HOD) introduced by Tinker & Wetzel (2010). This HOD reproduces well the angular correlation function of optical galaxies, red (star-forming) and blue (quiescent) galaxies at $0.4 < z < 2$. Therefore we make a strong assumption here, assuming that this description would work on star-forming galaxies. Given the current lack of understanding of the details of the process of star-formation and its evolution with redshift, it is difficult to define what would be a better HOD prescription and

we therefore stay with this one. We study power spectra coming from our model for several wavelengths/instruments: 100 μm IRAS, 160 μm Spitzer/MIPS, 250, 350, 500 μm Herschel/SPIRE and 850 μm, 1.3 and 2mm Planck/HFI. A list of the available data of CIBA power spectra is given in table 2.

3. The model

3.1. The parametric model of star-forming galaxies evolution

To reproduce the angular power spectrum of the CIBA we need a model for the redshift evolution of star-forming galaxies. We use the model presented in Béthermin et al. (2011). It is a backward evolution model based on a parametrized luminosity function and on galaxies spectral energy distribution templates.
Béthermin et al. (2011) consider a luminosity function (LF) that behaves like a power law for $L << L^\star$ and like a Gaussian for $L >> L^\star$ (Saunders et al. 1990) :

$$\Phi(L_{IR}) = \frac{dN(L_{IR})}{dV d\log_{10}(L_{IR})} \quad (1)$$

$$= \Phi^\star(z)\left(\frac{L_{IR}}{L^\star(z)}\right)^{1-\alpha} \exp\left[-\frac{1}{2\sigma^2}\log_{10}^2\left(1+\frac{L_{IR}}{L^\star(z)}\right)\right] \quad (2)$$

where $\Phi(L_{IR})$ is the number of galaxies with the infrared bolometric luminosity L_{IR} within the comoving volume dV and the bin $d\log_{10} L$. $\Phi^\star$ is a normalization constant that fixes the density of sources. The low and high luminosity parts have different slopes, $1-\alpha$ and $1-\alpha-1/\sigma^2/\ln^2(10)$ respectively. $L^\star$ represents the luminosity at the break. The parameters that describe the luminosity function are listed in table 1.
The luminosity function evolves with the redshift through $L^\star$ and $\phi^\star$:

$$L^\star(z) = L^\star(z=0)(1+z)^{r_L} \quad (3)$$

$$\phi^\star(z) = \phi^\star(z=0)(1+z)^{r_\phi} \quad (4)$$

Exponents r_L and r_ϕ are not identical for all z. Two breaks are imposed to reproduce the evolution of the LF. The first one z_{break} is a free parameter and is found to be around 1. The second one is fixed at $z = 2$ to avoid divergence at high z. Between these two breaks, the values of r_L and r_ϕ change as shown on table 1.

Béthermin et al. (2011) used the SED library of Lagache et al. (2004). It contains two galaxy populations: star-forming and late-type galaxies. The latter emit half or less of their energy in the IR whereas the former emit more than 95 % of their energy in the IR. The fraction of each population depends on luminosity. Indeed, late-type dominate at low luminosity whereas star-forming dominate at high luminosity. For a given bolometric luminosity, the fraction of star-forming is :

$$f_{SF} = \frac{\Phi_{SF}}{\Phi} \quad (5)$$

$$= \frac{1+\tanh[\sigma_{pop}(L)\log_{10}(L_{IR}/L_{pop})]}{2} \quad (6)$$

L_{pop} is the luminosity where $\Phi_{SF} = \Phi_{late-type}$ and σ_{pop} characterizes the width of the transition between the two populations.
Differential number counts are then derived for each population and then summed. At flux S :

$$\frac{dN}{dS}(S) = \int_z\int_L f_{pop}\frac{dN_{pop}}{d\log_{10} L_{IR} dV}\frac{d\log_{10} L_{IR}}{dS}\frac{dV}{dz}dz \quad (7)$$

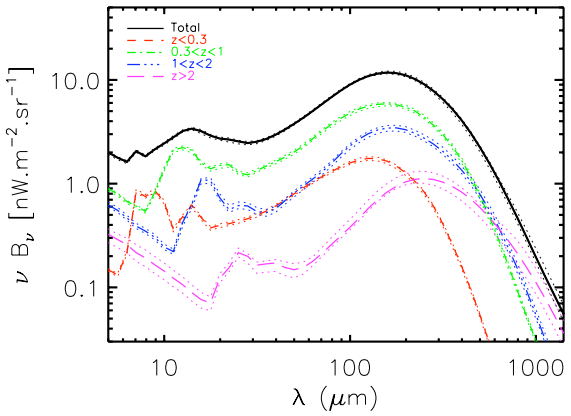

Fig. 1. CIB per redshift bins from the model of Béthermin et al. (2011). The high redshift contribution increases with the wavelength.

where dN/dS is the number of sources per flux unit in a unit solid angle and pop = late-type or pop = star-forming.
The model of Béthermin et al. (2011) is described by thirteen free parameters. Best fit parameters and confidence areas are computed using Monte-Carlo Markov Chains on available and trustworthy differential number counts and luminosity functions at certain wavelengths. Béthermin et al. (2011) fitted number counts of Spitzer/MIPS at 24, 70 and 160 μm (Béthermin et al. 2010), those of Herschel/SPIRE at 250, 350 and 500 μm (Oliver et al. 2010) and those of Aztec at 1.1 mm (Austermann et al. 2010; Scott et al. 2010). A couple of luminosity functions at different redshifts are also fitted, the 8 μm one at $z = 2$ from Caputi et al. (2007), others derived from Rodighiero et al. 2009 (a local LF at 24 μm, a 15 μm one at $z = 0.6$ and a 12 μm LF at $z = 1$) and that at 60 μm at $z = 0$ from Saunders et al. (1990). Moreover, absolute measurements of the CIB are also used as a model constraint (Lagache et al. 1999). We do not describe and discuss all the fits here (for a full discussion see Béthermin et al. 2011). Using the best fit, this model also provides the redshift distribution of the CIB as shown on Fig. 1. We see that higher-redshifts contribution increases with wavelength : the redshift slice $0.3 < z < 1$ dominates up to 400 μm whereas in the sub-millimeter $z > 2$ dominates. This model provides a very good agreement with the CIB redshift distribution (Jauzac et al. 2011). We will study how these thirteen free parameters can be constrained with power spectra of the CIBA.

3.2. The angular power spectrum

According to Haiman & Knox (2000), Knox et al. (2001) and using the Limber approximation, the angular power spectrum of the anisotropies of the CIB at wavelengths λ and λ' is :

$$C_\ell^{\lambda\lambda'} = \int dz \frac{dr}{dz}\frac{a^2(z)}{d_A^2}\bar{j}_\lambda(z)\bar{j}_{\lambda'}(z)P_{ss}(k=\frac{\ell}{d_A},z) \quad (8)$$

where ℓ is the multipole, r is the conformal distance from the observer, $a(z)$ the scale factor, d_A the comoving angular diameter distance, and $\bar{j}_\lambda(z)$ the mean emissivity per comoving unit volume at wavelength λ as a function of z. When $\lambda = \lambda'$ we recover the auto power spectrum. $P_{ss}(k)$ is the galaxy three dimensional power spectrum.

The emissivities are computed using the parametric luminosity functions following :

$$j_\nu(z) = \left(a\frac{d\chi}{dz}\right)^{-1} \int_L S(L_{IR}, z)\frac{dN}{dz d(lnL_{IR})} d(lnL_{IR}) \quad (9)$$

where $dN/dzd(lnL)$ is the number of galaxies per redshift bin dz and per luminosity bin $d(lnL)$ and S the flux. Each galaxy population (late-type and star-forming) emissivity are computed and summed to get the overall emissivity. Fig. 2 shows emissivities as a function of redshift. The two discontinuities at $z \sim 0.9$ and $z = 2$ are due to the breaks imposed by the parametrization of the model of galaxies. It is clear that as the wavelength increases, the contribution from the high redshift part increases. Emissivities are color corrected according to their instrument and wavelengths to give C_ℓ in Jy^2/sr (for the photometric convention νI_ν=cst).

In the context of the halo model, $P_{ss}(k)$ is the sum of the clustering in one single halo (1h) and in two different halos (2h):

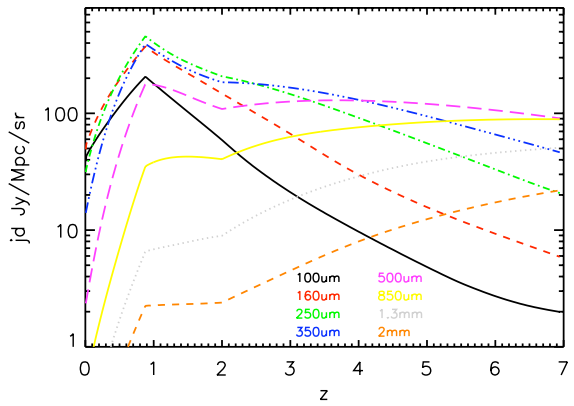

Fig. 2. Emissivities versus the redshift for different wavelengths. The contribution from high redshift increases with the wavelength.

$$P_{ss}(k) = P_{1h}(k) + P_{2h}(k) \quad (10)$$

where

$$P_{1h}(k) = \int_M \frac{dN}{dM}\frac{\langle N_{gal}(N_{gal}-1)\rangle}{\bar{n}^2_{gal}} U(k,M)^p dM \quad (11)$$

$$P_{2h}(k) = P_{lin}(k)\left[\int_M \frac{dN}{dM} b(M)\frac{\langle N_{gal}\rangle}{\bar{n}_{gal}} U(k,M) dM\right]^2 \quad (12)$$

. (13)

Here M is the halo mass, $P_{lin}(k)$ is the dark matter linear power spectrum (computed with the fit of Eisenstein & Hu 1998), $U(k, M)$ the normalized Fourier transform of the halo density profile that is assumed to be that of Navarro et al. (1996) truncated at the virial radius. $b(M)$ is the halo bias, $\langle N_{gal}\rangle$ the probability of having N_{gal} galaxies in a halo of mass M and we consider $p = 2$ (Cooray & Sheth 2002). The mean number density of galaxies $\bar{n}_{gal}$ is given by:

$$\bar{n}_{gal} = \int \frac{dN}{dM}\langle N_{gal}\rangle dM \quad (14)$$

where dN/dM is the halo mass function. We will use the universal form given by Tinker et al. (2008) as well as its redshift evolution. We use its associated halo bias (see Eq. A1 in Tinker et al. (2009)).

The halo occupation number introduces galaxies in the halos statistically. Recent data and simulations suggest a necessary distinction between the major galaxy that lies at the center of the halo and the satellite galaxies that populate the rest of the halo. Above a given mass threshold, most halos will host a central galaxy. Above a second higher mass threshold, they will also host satellite galaxies. N_{gal} can thus be written as :

$$\langle N_{gal}\rangle = \langle N_{cen}\rangle + \langle N_{sat}\rangle \, . \quad (15)$$

According to the prescription of Tinker & Wetzel (2010), the occupation function of central galaxies is:

$$\langle N_{cen}\rangle = \frac{1}{2}\left[1 + \mathrm{erf}\left(\frac{\log M - \log M_{min}}{\sigma_{\log M}}\right)\right] \quad (16)$$

where M_{min} is the halo mass at which a halo has a 50 % probability of hosting a central galaxy. $\sigma_{\log M}$ controls the width of the transition between zero and one central galaxy. There is a smooth transition between low mass halos that do not contain bright enough galaxies to be seen in the data ($M << M_{min}$) and more massive ones that always contain a bright central galaxy. ($M >> M_{min}$). The satellite occupation function is:

$$\langle N_{sat}\rangle = \frac{1}{2}\left[1 + \mathrm{erf}\left(\frac{\log M - \log 2M_{min}}{\sigma_{\log M}}\right)\right]\left(\frac{M}{M_{sat}}\right)^{\alpha_{sat}} \quad (17)$$

It has a cut-off of the same form as the central occupation with a transition mass twice larger than that of the central to prevent halos which have a low probability of hosting a central galaxy to contain satellite galaxies. The number of satellite galaxies grows with a slope of α_{sat}. Both number of galaxies as well as their sum are plotted on Fig. 3.

With this model, the angular power spectrum of CIBA depends on only four halo model parameters α_{sat}, M_{min}, M_{sat} and σ_{logM}. Cosmology is fixed at WMAP7 values. Our parameters are listed in Table 1 with their meaning and their fiducial values that we set in Sect. 4 .

The long term purpose of our model is to look for best fits of these parameters for Spitzer/MIPS, IRIS, Planck, Herschel and SPT data and study their evolution with wavelength. However it is beyond the scope of this paper. **Therefore we will not compare the data to the power spectra coming from our model**. Our first aim here is to study the parameter space and to investigate particularly the behaviour of the halo bias, the halo mass-contribution to the power spectrum and its redshift distribution. To do so we will consider a set of fiducial halo parameters identical at all wavelengths.

4. Power spectra and parameters degeneracies

In this section, we present the CIB power spectra computed with the model detailed in the previous section for several wavelengths in the far-IR and sumillimeter. We then study the degeneracies of the parameters, looking first at the galaxies model parameters and second at the HOD parameters.

4.1. Power spectra

Our fiducial model is set with the HOD parameters $\log M_{min} = 11.5$, $M_{sat} = 10M_{min}$ and $\alpha = 1.4$ at all wavelengths. These values are motivated by the parameters fit of

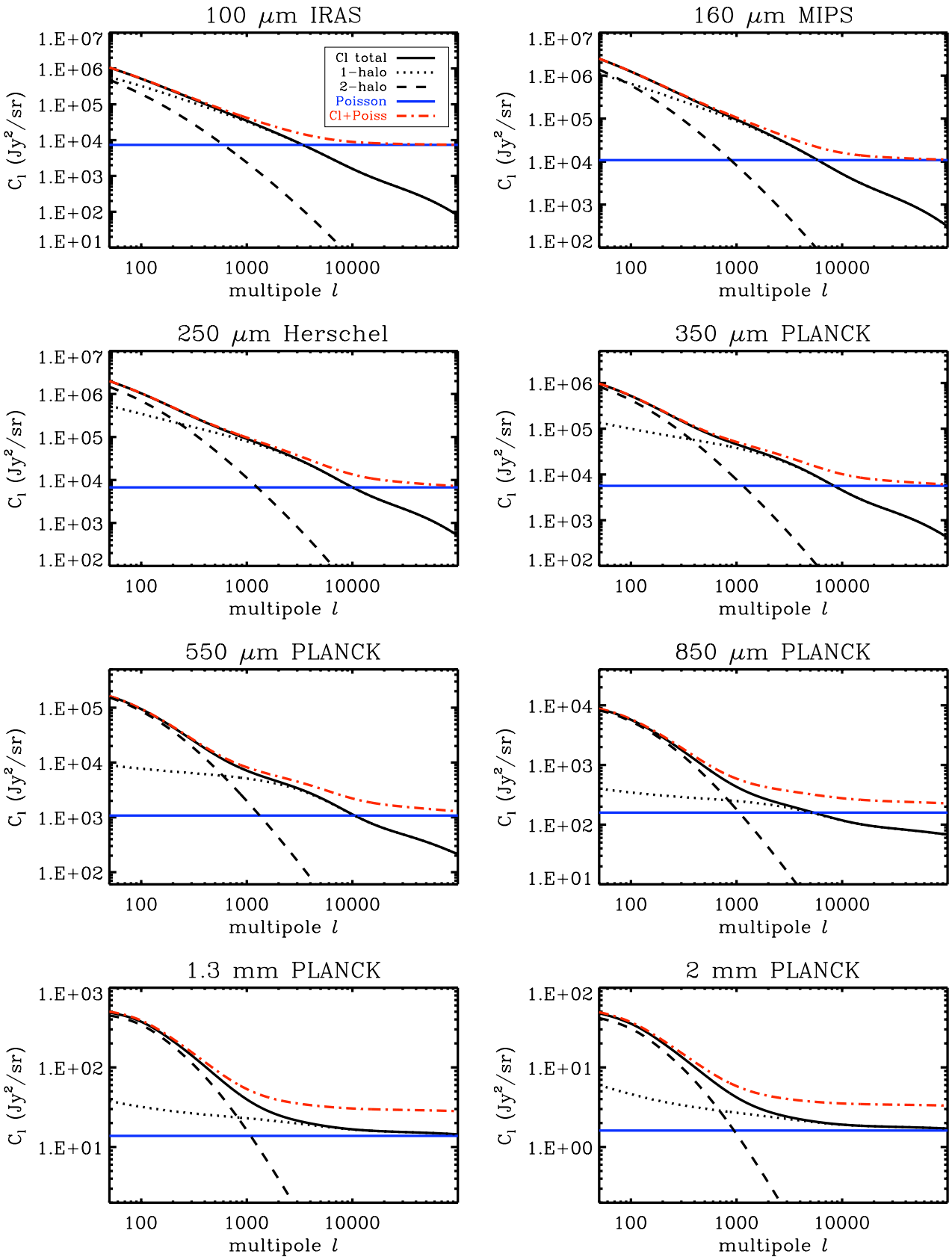

Fig. 4. CIB anisotropies power spectra at several wavelengths. The continous black line shows the power spectra of the clustering. The dotted black line is the 1-halo term of the power spectrum and the dashed line is the 2-halo term. The blue horizontal line represents the shot noise level and the red dot-dashed curve is the total power spectrum. Titles of the plots give the reference for the shot noise level and the used bandpass filters.

parameter name	Description	Value
M_{min}	Minimal mass of a halo to have a central galaxy	$10^{11.5} M_\odot$
M_{sat}	Nomalisation mass for satellite galaxies	$10^{12.5} M_\odot$
α_{sat}	Slope of the number of satellite galaxies at high mass	1.4
σ_{logM}	Scatter in halo mass	0.748
α	Faint end slope of the IR bolometric LF	1.223
σ	Parameter driving the bright end slope	0.406
$L_\star$(z=0)	Local characteristic luminosity of the LF	$2.377\times10^{10} L_\odot$
$\phi_\star$(z=0)	Local characteristic density of the LF	3.234×10^{-3}gal/dex/Mpc^3
$r_{L_\star,lz}$	Evolution of the characteristic luminosity between 0 and z_{break}	2.931
$r_{\phi_\star,lz}$	Evolution of the characteristic density between 0 and z_{break}	0.774
z_{break}	Redshift of the first break	0.879
$r_{L_\star,mz}$	Evolution of the characteristic luminosity between z_{break} and 2	4.737
$r_{\phi_\star,mz}$	Evolution of the characteristic density between z_{break} and 2	-6.246
$r_{L_\star,hz}$	Evolution of the characteristic luminosity for $z > 2$	0.145
$r_{\phi_\star,hz}$	Evolution of the characteristic density for $z > 2$	-0.919
L_{pop}	Luminosity of the transition between normal and star-formig templates	23.677×10^{10}
σ_{pop}	Width of the transition between normal and star-forming templates	0.57

Table 1. Parameters of our model. The first part of the table lists the halo model parameters and the second part lists the parameters of the model of galaxies. The values of the latter are the mean ones of Béthermin et al. (2011).

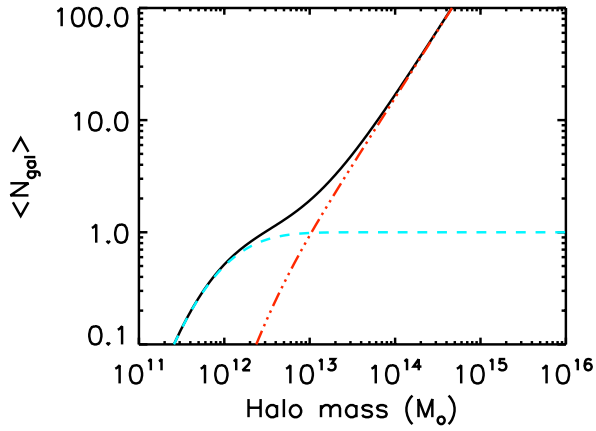

Fig. 3. Number of galaxies versus dark matter halo mass. The blue dashed line shows the central galaxies, the red dotted-dashed line shows satellite galaxies and the black continuous line shows the total. We use the parameters of our fiducial model (see Sect. 4), that is to say $\log M_{min} = 11.5$, $M_{sat} = 10 M_{min}$ and $\alpha = 1.4$

Viero et al. (2009), Planck Collaboration et al. (2011), Amblard et al. (2011). As the halo parameters slightly depend on the wavelength (in reality but it is not the case here), the power spectra presented in this section may not be seen as an exact prediction but as a basis for a qualitative study. For this fiducial model, we present on Fig. 4 the power spectra for different experiments and selected wavelengths, from 100 μm to 2 mm.

The comparison to measurements also requires the introduction of a shot noise term due to the finite number of galaxies. We compute it using our galaxy evolution model (Béthermin et al. 2011).

$$C_\ell = C_{\ell,clus} + C_{\ell,shot} \tag{18}$$

where $C_{\ell,clus}$ is the power spectrum of the clustering and $C_{\ell,shot}$ is the shot noise. $C_{\ell,shot}$ depends on the flux cut applied to the data when removing or masking the brightest sources. Typical flux cuts for different far-IR and sub-millimeter experiments are given in Tab. 2. On Fig. 4, we only show one shot noise level per wavelength corresponding to the instrument given in the plot titles, for purpose of clarity.
The contribution of the 1-halo (2-halo) corresponds to the dotted line (dashed line). The instrument noise is not shown here but it is often negligible, the CIB being measured with a very high S/N even at spatial scales close to the angular resolution. Looking at this plot, we see clearly that the interplay between 2h, 1h and shot noise terms will make the interpretation of measurements quite subtle. The contribution of the 1-halo term decreases with the wavelength which can prevent its measurement if the resolution of the instrument is low. For example, Planck with its 5 ′angular resolution at high frequency, cannot measure directly the shot noise level and the 1-halo term can be easily misinterpreted as shot noise. Reversely, the 1-halo term dominates a large range of scales at 100 and 160 μm and thus can be measured accurately at these wavelengths.
High wavelengths probe higher redshifts than short ones and halos are relatively smaller at high redshifts compared to those in the local Universe as the latter had time to accrete more matter. Therefore the scale of the intersection between the 1- and 2-halo terms shifts towards higher ℓ as the wavelength increases. It goes from $\ell \sim 50$ at 100 μm to $\ell \sim 1000$ at 2 mm. Viero et al. (2009) also observed this trend. At 250 μm the crossing is at $k \sim 0.03$ arcmin^{-1} ($\ell \sim 648$) whereas it is at $k \sim 0.06$ arcmin^{-1} ($\ell \sim 1296$) at 500 μm. The exact crossing point differs from ours because of the HOD parameterization.

4.2. Variation of power spectra with the galaxy-evolution model parameters

In order to do an overall study of how our model parameters can be constrained, i.e. to investigate how degenerated they are, we construct the Fisher matrix associated to the power spectra. We write the Fisher matrix for angular power spectrum measurements as:

$$F_{ij} = \sum_\lambda \sum_\ell \frac{1}{\sigma_\ell^{\lambda 2}} \frac{\partial C_\ell^\lambda}{\partial \theta_i} \frac{\partial C_\ell^\lambda}{\partial \theta_j} \tag{19}$$

wavelength (μm)	Instrument	Reference	Flux Cut (mJy)	Shot noise level (Jy^2/sr)
100	IRIS	Pénin et al. (2011)	700	7364±1232
160	Spitzer/MIPS	Lagache et al. (2007)	200	10834±3124
250	Herschel/SPIRE	Amblard et al. (2011)	50	6715±1458
350	Herschel/SPIRE	Amblard et al. (2011)	50	4362±1250
350	Planck/HFI	Planck Collaboration et al. (2011)	710	5923±367
500	Herschel/SPIRE	Amblard et al. (2011)	50	1156±434
550	Planck/HFI	Planck Collaboration et al. (2011)	540	1150±92
850	Planck/HFI	Planck Collaboration et al. (2011)	325	138±22
1363	SPT	Hall et al. (2010)	6.4	11.9±4.0
1363	ACT	Fowler & Atacama Cosmology Telescope Team (2010)	20	12.5±3.9
1380	Planck/HFI	Planck Collaboration et al. (2011)	160	12.9±2.9
2000	SPT	Hall et al. (2010)	6.4	1.73±0.54
2000	ACT	Fowler & Atacama Cosmology Telescope Team (2010)	20	1.78±0.60
2097	Planck/HFI		245	1.4±0.3

Table 2. Shot noise levels in Jy^2/sr from Béthermin et al. (2011) for available measurements of CIBA power spectra.

wavelength (μm)	Instrument	Jy^2/sr to μK$^2_{CMB}$
100	IRAS	9.59×10^{22}
160	Spitzer/MIPS	3.12×10^{11}
250	Herschel/SPIRE	1.34×10^{3}
350	Herschel/SPIRE	2.78×10^{-1}
350	Planck/HFI	2.00×10^{-1}
500	Herschel/SPIRE	7.45×10^{-4}
550	Planck/HFI	2.94×10^{-4}
850	Planck/HFI	1.20×10^{-5}
1380	SPT	4.39×10^{-6}
1380	Planck/HFI	4.32×10^{-6}
2000	SPT	6.10×10^{-6}
2097	Planck/HFI	7.31×10^{-6}

Table 3. Conversion factors from Jy^2/sr to μK$_{CMB}$. One should multiply the power spectrum in Jy^2/sr (with the convention νI_ν =cst) by the coefficient to get μK$^2_{CMB}$.

where σ_ℓ are the errors on the measurements and they include both the cosmic variance and the instrumental noise at a multipole ℓ:

$$\sigma_\ell^2 = \left(C_\ell + \frac{N_\ell}{B_\ell^2}\right)^2 \frac{2}{f_{sky}(2\ell+1)} \quad (20)$$

where f_{sky} is the fraction of the sky we consider, N_ℓ is the level of the instrumental noise and B_ℓ^2 the power spectrum of the beam. To compute the Fisher matrices, we generate mock power spectra using our fiducial model and error bars derived following Eq. (20), from 100 μm to 1.3 mm. The range of multipoles is taken to be consistent with the available data. At 350 and 550 μm, we assume combined power spectra for Planck and Herschel, and we thus extend Planck power spectra to the Herschel limit in multipole. We plot C_ℓ in Jy^2/sr. They can be converted in μK^2 using the coefficients given in Tab. 3.

The bottom left panel of Fig. 5 shows confidence ellipses (1σ in green and 2σ in black) coming from C_ℓ when trying to measure only the galaxy model parameters $r_{L^\star,hz}$ and $r_{L^\star,lz}$. Clearly, they are very poorly constrained. For instance $r_{L^\star,hz}$ = 0.145±15.55, or $r_{L^\star,lz}$ = 2.93±20.0. For reference, the constraints obtained using current number counts are $r_{L^\star,hz}$ = 0.145±1.05 and $r_{L^\star,lz}$ = 2.93±0.27, as shown on the top left panel of Fig. 5. The fact is that these parameters enter in the expression of the C_ℓ through the emissivities which are integrated on all redshifts, they are thus hard to measure from clustering measurements alone.

As a matter of fact, the lack of information in C_ℓ partially comes from the large number of parameters in the model of evolution of galaxies. To quickly quantify this we vary only a few of these parameters ($r_{L\star,lz}$, $r_{L\star,hz}$, z_{break}, $r_{\phi\star,lz}$ and $r_{\phi\star,hz}$) assuming that the others are perfectly known. Fixing all but these parameters corresponds to assuming that only the redshift evolution of the LF is unknown, clearly an irrealistic assumption. Not surprisingly, while some of the degeneracies remain in these reduced parameter space, on the whole, parameters are better contrained. For instance, we now obtain $r_{L^\star,lz}$ = 2.93±0.10 and $r_{L^\star,hz}$ = 0.145±7.05 which are about a two order of magnitude and a factor 2 improvement, respectively as compared to the numbers above.

In order to illustrate further this lack of information in C_ℓs, we show how they change with only one parameter, $r_{L^\star,lz}$. We make it vary by $\pm2\sigma$ from its best fit (σ coming from Béthermin et al. 2011). This parameter governs the evolution of the luminosity function for $0 < z < z_{break}$. A higher $r_{L^\star,lz}$ means a faster increase of the luminosity, thus a higher value of $L^\star(z = z_{break})$. The top panel of Fig. 6 shows the influence of this parameter on the counts at 160 μm. A higher (smaller respectively) $r_{L^\star,lz}$ implies higher (smaller) number counts thus more (less) galaxies on a large range of fluxes. This leads to a higher (smaller) emissivities as shows in the second and third panels of Fig. 6. This results in a modification of $\sim$ 20% on the emissivities and from 15 to 35 % on power spectra depending on the scale. The fact that this ratio is not constant is due to to the fact that the ratio of the emissivities is not constant with redshift (3rd panel of Fig. 6). We can see that all power spectra are consistent within error bars and thus we can hardly discriminate between them. Therefore, it is hard to constrain the evolution model of galaxies using only power spectra.

More relevant data are required. We compare our confidence ellipses with those obtained with luminosity functions and number counts data. To do so we use the covariance matrix of Béthermin et al. (2011). The error bars are in general much smaller and there are only a few degeneracies. For instance, as shown on the left panel of Fig. 5, $r_{L^\star,hz}$ and $r_{\phi^\star,hz}$ are still strongly degenerate but they are now much better constrained.

So far, we have investigated how galaxy evolution parameters are degenerated and constrained using LF/counts and C_ℓ separately. The next step is to look at the degeneracies when combining all these data. To do so, we add the two Fisher matrices coming from the counts/LF and the C_ℓ. The bottom panels of Fig. 5 show the confidence ellipses for $r_{L^\star,hz}$, $r_{L^\star,lz}$ and $r_{\phi^\star,hz}$ using the combined data. Note that the axis scales are different. The con-

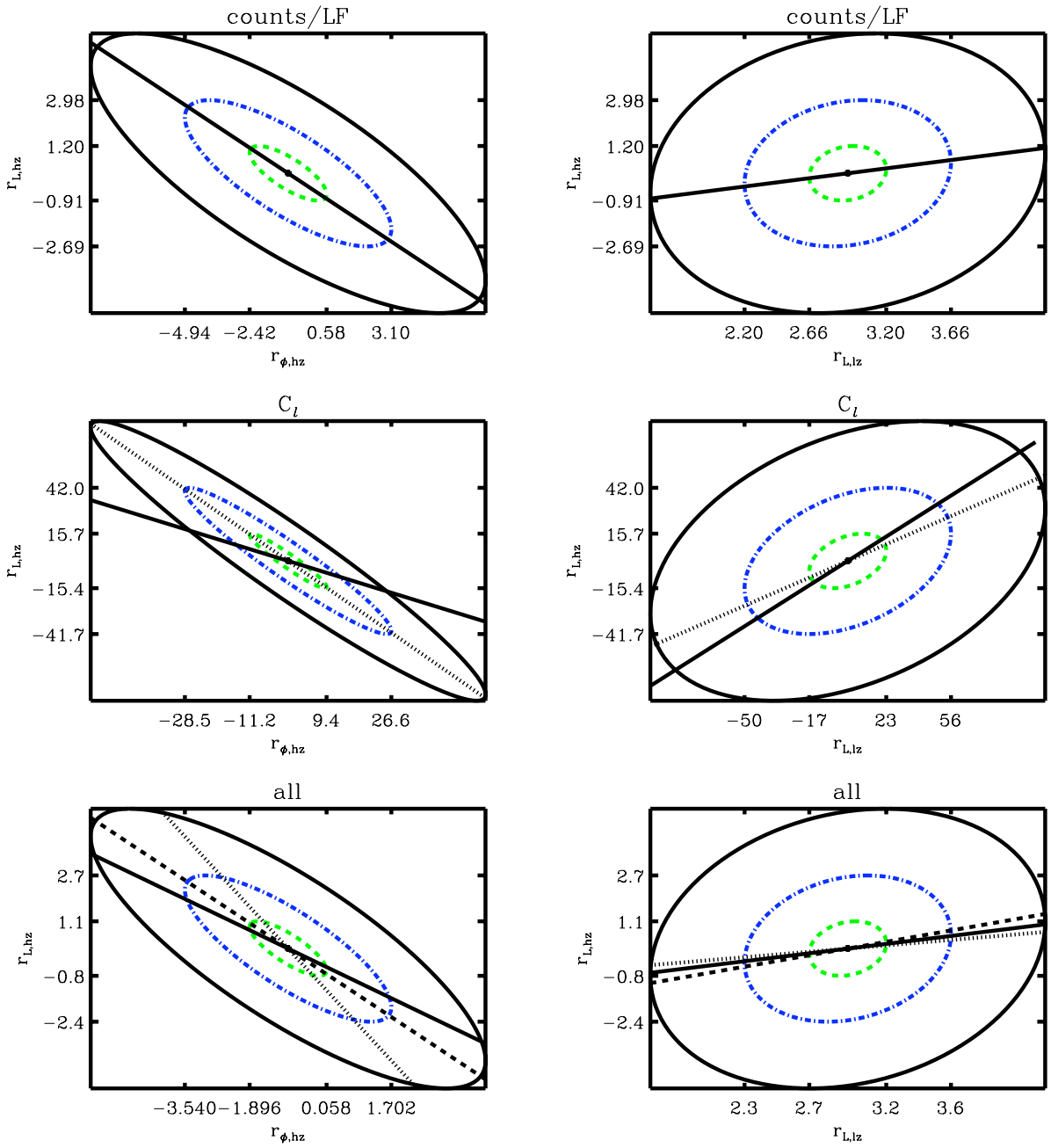

Fig. 5. 1σ (dashed green), 2σ (dash-dot blue), 3σ (black) likelihood contours of the galaxy evolution model parameters $r_{L^\star,hz}$, $r_{L^\star,lz}$ and $r_{\phi^\star,hz}$. Top, Middle and Bottom panels show the contours computed using counts/LF data, C_ℓ data only, and combined counts/LF and C_ℓ data, respectively. The continous line shows the direction of degeneracy using only counts/LF, the dotted line shows that using C_ℓ and the dashed line is that using all data. C_ℓ alone cannot constrain the galaxy-evolution model parameters and the combination of C_ℓ and counts/LF data do not change much the constraints. It slightly improves them.

tinous/dashed/dotted lines on Fig. 5 indicate the degeneracy directions. They are different which illustrate the complementarity of the two data-sets and the constraints can be greatly improved. For example, the errors on $r_{\phi^\star,hz}$ are decreased by a factor of 1.5 but the errors on $r_{L^\star,hz}$ is not changing. However, this plot also clearly shows that overall, the number counts and LF measurements are much more powerful when looking at constraining the LF. However, C_ℓ can still constrain the global evolution of galaxies through their mean emissivities. A first attempt was made by Amblard et al. (2011) who did not use a model of galaxies to compute the emissivities but bin them in several redshift intervals and considered the values of the emissivities in these four bins as free parameters. They also required that the integrated source density is within the 68% confidence level ranges of the CIB obtained by FIRAS.

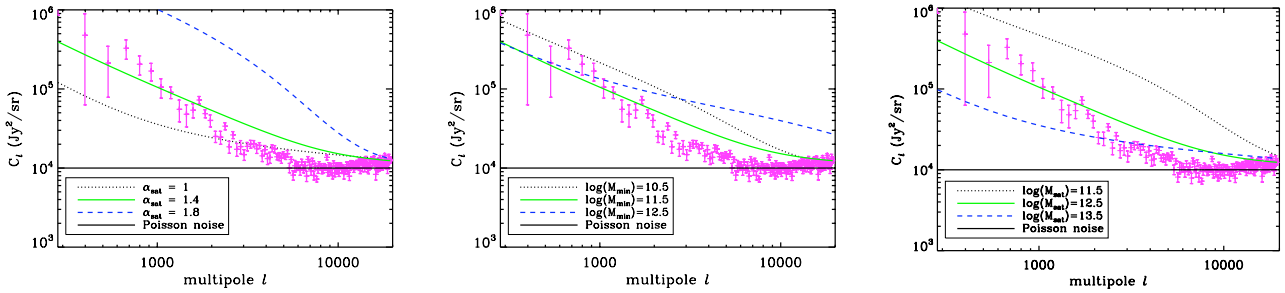

Fig. 7. CIBA power spectrum at 160 μm obtained using several values of α_{sat},M_{min} and M_{sat}. The level of the Poisson noise has also been added to the power spectra (black continous line). Pink dots are the data from Lagache et al. (2007) at 160 μm. When fixed, the parameters are those of the fiducial model, $\alpha_{sat} = 1.4$, $M_{min} = 10^{11.5} M_\odot$ and $M_{sat} = 10^{12.5} M_\odot$. Left panel: The blue line is for $\alpha_{sat} = 1.8$, the green one for $\alpha_{sat} = 1.4$ and the black one for $\alpha_{sat} = 1$. Middle panel: The blue line is the clustering power spectrum for $M_{min} = 10^{12.5} M_\odot$, the green one for $M_{min} = 10^{11.5} M_\odot$ and the black one for $M_{min} = 10^{10.5} M_\odot$. Right panel: The blue line is for $M_{sat} = 10^{13.5} M_\odot$, the green one for $M_{sat} = 10^{12.5} M_\odot$ and the black one for $M_{sat} = 10^{11.5} M_\odot$. As expected, C_ℓs strongly depend on the halo parameters. We can expect strong degeneracies between those parameters.

4.3. Halo occupation distribution parameters and their degeneracies

The shape of the clustering power spectra strongly depends on the HOD parameters as shown on Fig. 7. We vary M_{min}, M_{sat} and α_{sat}. Each panel shows the power spectrum at 160 μm measured by Lagache et al. (2007) in addition to the ones coming from the model. In each plot we vary only one HOD parameter and hold the others fixed to the values of the fiducial model, $\alpha_{sat} = 1.4$, $M_{min} = 10^{11.5} M_\odot$ and $M_{sat} = 10^{12.5} M_\odot$. Both the shape and amplitude strongly vary. The fact that some similar changes are observed using different parameters suggest strong degeneracies. We compute the Fisher matrix as in Sect. 4.2 and likelihood contours at 1- and 2-σ are shown on Fig. 8. The error bars on σ_{logM} are very large, thus we fix its value to 0.65, following Tinker & Wetzel (2010) who studied the galaxy-clustering in optical surveys. Using C_ℓ only we are not able to constrain its value. M_{min} and M_{sat} happen to be highly degenerated in the direction $M_{sat} = 3.3 M_{min}$.

In previous works using optically selected galaxies, α is usually set to 1 (Gao et al. (2004)) and M_{min} and M_{sat} are the only parameters to be fitted to the data. Indeed, α is hardly constrained. For instance Tinker & Wetzel (2010) used the same halo distribution number on a sample of red and blue galaxies in the range $0.4 < z < 2$. They fitted well their correlation function fixing $\alpha = 1$ and letting free M_{min} and M_{sat}. But when they let α free in addition to the two others, they obtain unrealistic values for α (Tinker & Wetzel 2010). However, setting $\alpha = 1$ might not be appropriate for CIBA. The halo model is commonly used in galaxies catalogs that are not deeper than $z \sim 2$ and CIBA probe higher redshifts, especially at long wavelengths. Moreover optically-selected galaxies are not only star-forming galaxies, and there is no reason why optically-selected galaxies and star-forming galaxies should behave in the same way. Magliocchetti et al. (2008) used a similar form of the halo model to analyze the angular correlation function of 24 μm sources at $0.6 < z < 1.2$ and $z \geqslant 1.6$. Using two halo density profiles (NFW and a steeper one $\rho \sim r^{-3}$), they derived $\alpha \sim 0.7$ for the steeper profile and $\alpha \sim 0.8$ for the NFW one. They get the same results for both sets of data. On the contrary, Cooray et al. (2010) computed the angular correlation function of sources detected at 250, 350 and 500 μm in Herschel/SPIRE data. They used the same halo distribution as ours and get $\alpha = 1.3 \pm 0.4$, $\alpha < 1.8$ and $\alpha < 1.6$ at 250, 350 and 500 μm respectively. Finally, the Planck Collaboration et al. (2011) derived values of α compatible with 1. The discrepancy with Magliocchetti et al. (2008) may be due to the different properties of the bright galaxies selected at 24 μm and those that contribute to the CIBA at longer wavelengths. Here combining all CIBA measurements from 100 μm to 1.3 mm and low to high multipoles, α is well constrained and it is not strongly degenerated with other parameters. Note that values of $\alpha > 1$ implies that higher-mass halos contribute relatively more than smaller-mass ones compared to the halos in which lie optical galaxies such as those used by Tinker & Wetzel (2010).

In our analysis of the degeneracies of the halo parameters we have only considered a set of parameters identical for all wavelengths which is not the case in reality. It could thus be that the degeneracies depend on wavelength. We therefore checked that the degeneracies were not significantly changing when we compute the Fisher matrix with various set of parameters corresponding to the wavelength best-fit models.

The halo parameters cannot be constrained by counts or LF as they only intervene in the clustering of galaxies in the equation of the C_ℓ (see Eq. 8). Therefore we cannot carry a joint analysis of the degeneracies of the halo parameters using counts/LF and C_ℓ data all together. Note that in principle, we could extrapolate the number count measurements to constrain the total number of galaxies, which also depends on the HOD parameters, but this would be a difficult measurement as it would be strongly dependent on the flux cut, for example.

Emissivities are given by the model of galaxy evolution but we want to investigate the degeneracies if they are binned in redshift and their values considered as free paramete,rs as in Amblard et al. (2011). They carried this analysis at redshift between 0 and 4. In order to be coherent with what has been done previously and to take advantage of our redshift range, from 0 to 7, we split the whole redshift range in four bins, $0 < z < 0.9$, $0.9 < z < 2$, $2 < z < 3.5$, $3.5 < z < 7$. For each bin i we take the mean value of the emissivity that we call $b_{j,i}$ with $i = \{1, 2, 3, 4\}$ and we compute the C_ℓ at 350 μm (we assume a combined Planck and Herschel power spectrum) and the associated Fisher matrix. Confidence levels are given on Fig. 9. First we see that the halo occupation number degeneracies do not change much (see the previous paragraph) apart from the error bars which are much larger. M_{min} is still strongly degenerated with M_{sat} such as $M_{sat} = 2.7 M_{min}$. The direction of the degeneracy is roughly

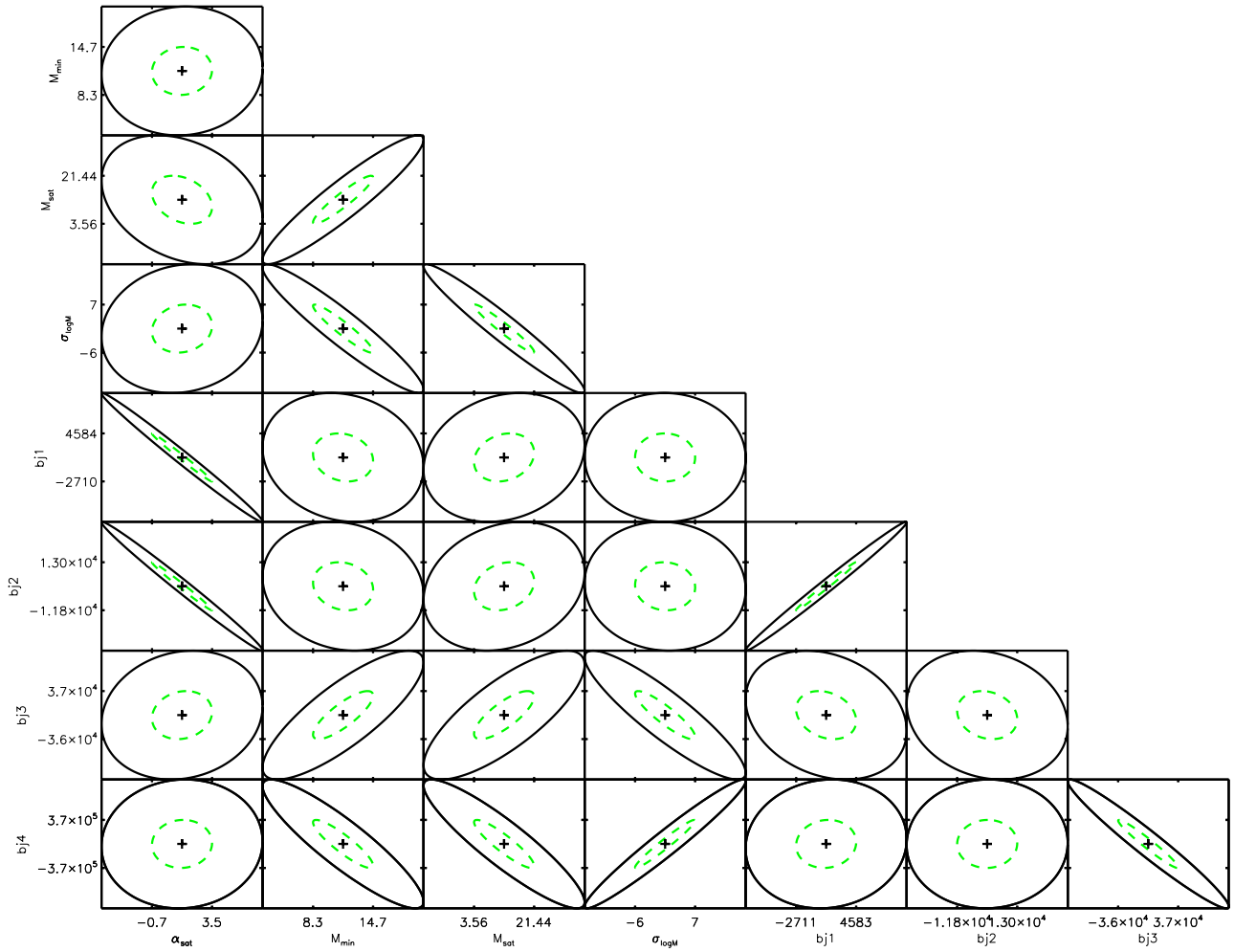

Fig. 9. 1σ (green) and 2σ (black) likelihood contours of the halo model parameters computed with mock data at 350 μm. Instead of using emissivities coming from the model of galaxies, we split C_ℓ in four redshift bins, on which we use the mean value of the emissivity on each bin $b_{j,i}$ that we consider as free parameters. The $b_{j,i}$ are hardly constrained with our data. α_{sat} is strongly degenerate with $b_{j,1}$ and $b_{j,2}$ which are the mean emissivities at low z. M_{min} M_{sat} and σ_{logM} are degenerate with $b_{j,3}$ and $b_{j,4}$, the mean emissivities at high z.

the same as that derived using emissivities of the model as well as those of σ_{logM} and M_{sat} and M_{min}. Therefore, the degeneracy directions are all similar, using the emissivities or letting them free.

The degeneracies of the b_j with the halo parameters depend on the redshift. Indeed, α_{sat} is highly degenerated with b_{j1} ($0 < z < 0.9$) and b_{j2} ($0.9 < z < 2$) and not at all with b_{j3} ($2 < z < 3.5$) and b_{j4} ($3.5 < z < 7$). Therefore α_{sat} is constrained by $z > 2$ galaxies whereas the other halo parameters behave in the opposite way, they are not degenerate with b_{j1} and b_{j2} but with b_{j3} and b_{j4}. This redshift dependency is emphasized by their own degeneracies. b_{j1} and b_{j2} are strongly correlated, the same is true for b_{j3} and b_{j4}. The degeneracies using other wavelengths are only slightly different, we do not show them here. In general, the couples (b_{j1}, b_{j2}) and (b_{j3}, b_{j4}) are always strongly degenerate and the $b_{j,i}$ are degenerate with the halo parameters as shown on Fig. 9. Such a degeneracy dependence with the redshift has to be still understood.

In order to compare our results with those of Amblard et al. (2011), we carry a similar analysis using their redshift bins, that is to say, $0 < z < 1$, $1 < z < 2$, $2 < z < 3$ and $3 < z < 4$. We observe the same behavior as described previously but different from their results. They used Monte Carlo Markov Chains to compute the degeneracies and usually the two dimensional probability distributions have two peaks (see their fig. S 13). Their S_i are equivalent to our $b_{j,i}$. S_1 is degenerate with the three others S_i, whereas there is no degeneracy between S_3 and S_4. We do not discuss the degeneracy of the halo parameters with S_i as their parameterization of the halo occupation number slightly differ from ours.

Using $b_{j,i}$ and fitting them on the data avoids us to rely on a model of evolution of galaxies. However they are poorly constrained with the present data. Moreover the degeneracies between the $b_{j,i}$ and the halo parameters strongly depend on the halo parameterization used.

5. Interpreting measurements

Now that we have determined a model and the associated parameters degeneracies, we discuss their physical interpretation.

5.1. Redshift and halo-masses contribution to the power spectrum

The left panel of Fig. 15 shows the contribution to the C_ℓ by several redshift bins. As stated previously, the shorter the wavelength, the more important is the relative contribution from the low redshift. For example, while $z < 0.7$ contributes significantly at 100 and 160 μm, it becomes much less important in the millimeter range. Reversely, the high redshift bin ($z > 3$) is negligible at short wavelength but has an increasing contribution when the wavelength increases. The redshift distribution can change with the choice of the halo parameters as shown on Fig. 11. We have changed the values of α_{sat} on the left panels and that of M_{min} on the right panels (the change is in the 1σ error bars of the best fit found by Planck Collaboration et al. (2011)), the other parameters are those of the fiducial model. We recover the trend noticed above more or less emphasized.
Further, not only the redshift of the galaxies probed depends on the wavelength, but so does the mass of the halos in which they are embedded. Fig. 10 shows the contribution of mass and redshift to the 1- and 2-halo terms (at $\ell = 2002$ and $\ell = 100$ respectively) from 100 μm to 2 mm. High-mass halos ($M > 10^{13} M_\odot$) contribute the more to the 1-halo term from 100 μm to 2 mm at low redshift, and this dominant mass range stays constant with wavelength. More massive halos contain more galaxies than smaller ones therefore the galaxies contained in those halos contribute more to the angular power spectrum. This can be explained qualitatively in the following way. According to the mass function, at say $z = 0.5$, there are one thousand times more halos of $M = 10^{11} M_\odot/h$ than halos of mass $M = 10^{14} M_\odot/h$. According to the HOD, one out of one hundred $10^{11} M_\odot/h$ halo hosts a galaxy, whereas $M = 10^{14} M_\odot/h$ mass halos hosts on average 10 galaxies. Since the contribution to the 1-halo terms goes like N_{gal}^2, lore massive halos contribute relatively more to the 1-halo term. Note that this trend is less prononced for the 2-halo term since it goes like N_{gal}. At all wavelengths, as the redshift increases, the dominant mass range decreases to $M \sim 10^{11-13} M_\odot$ as halos at higher redshifts are smaller than those at $z = 0$.
The 2-halo term does not exhibit the same behavior : at short wavelengths, halos in a large range of mass $10^{11} - 10^{15} M_\odot$ at low z contribute to the power spectrum. In parallel, intermediate masses contribute at higher z. As the wavelength increases, the relative contribution between high mass at low z and intermediate mass at high z becomes close to unity. It ends up in an equal contribution from high mass at low z and from intermediate mass at high z at 2 mm. Intermediate mass halos are more abundant which explains their high contribution. Both the 1 and 2-halo terms are sensitive to different mass regimes which evolve with the wavelength and thus with the redshift.
Magliocchetti et al. (2008) selected 24 μm sources at $1.5 < z < 3$ and deduced from their correlation function that they lie in $10^{13} M_\odot$ halos. Viero et al. (2009) found an $M_{eff} \sim 10^{13.2} M_\odot$ for unresolved galaxies at $z > 1$ at 250, 350 and 500 μm. Brodwin et al. (2008) derived the angular autocorrelation function of dust-obscured galaxies selected with a color criterion. They determined that they are in halos with an average mass of $10^{12.2} M_\odot$. Gilli et al. (2007) selected star forming galaxies at 24 μm, derived the projected correlation function and found that LIRGs lie in halos $M > 3 \times 10^{13} M_\odot$. All these results are in agreement with ours. Overall, halos with masses such as $10^{12-13} M_\odot$ contribute the most to power spectra at all redshifts. However, we want to reemphasize here that these conclusions are model-dependent and depend on the particular emissivity model used, as discussed before. This is particularly true for the higher-z contribution, say $z > 2$.

5.2. Linear bias

Within our halo model we derive the linear bias as a function of the redshift following:

$$b_{lin}(k,z) = \sqrt{\frac{P_{gg}(k,z)}{P_{lin}(k,z)}} \tag{21}$$

where $P_{gg}(k,z)$ is the galaxy-galaxy power spectrum coming from our model, $P_{lin}(k,z)$ is the linear DM power spectrum and $b_{lin}(k,z)$ the linear bias.
We will call the effective bias coming from the HOD model, b_{HOD}. On large scale $u(k \to 0, M) \sim 1$, so the HOD bias from Eq. 13 is :

$$b_{HOD}(z) = \int dM \frac{dN}{dM} b(M) \frac{< N_{gal} >}{\bar{n}_{gal}} \tag{22}$$

We plot in Fig. 12 the linear biases and the HOD bias for our fiducial model as a function of redshift for $k = 1$ (Mpc/h)$^{-1}$ and $k = 10^{-2}$ (Mpc/h)$^{-1}$ where we also add current measurements detailed in Tab. 4. Note that in the linear regime, the HOD and linear biases are identical which is the case at $k = 10^{-2}$ (Mpc/h)$^{-1}$ but not at $k = 1$ (Mpc/h)$^{-1}$. On small spatial scales, the $u(k \to 0, M) \sim 1$ is not true therefore it is strongly different from the linear bias for $k = 1$ as shown on Fig. 12.
For both scales, our linear biases as well as the HOD bias is not in agreement with measurements. Neither of them show the same trend as the data points. The measured linear biases as well as the HOD biases grow quicker towards higher values than the biases extracted from our model.
HOD bias measurements are from different HOD. Cooray et al. (2010) used the same halo occupation number to fit the correlation function and they found different parameters than ours. When using their parameters set, we do recover their results. The discrepancy could be explained by the fact that these measurements result from correlation function analysis, thus from resolved sources which is not the population we are studying here.
Concerning the linear bias determined with unresolved galaxies (Lagache et al. 2007; Viero et al. 2009), our linear bias is not in agreement with the measurements either. Indeed when using unresolved sources, the determination of the bias requires the use of emissivities, which are strongly model dependent (see Sect. 5.3) and it can affect the bias.

5.3. Influence of the mean emissivities

Previous models such as those of Lagache et al. (2007) and Viero et al. (2009) have used emissivities coming from Lagache et al. (2004). In Fig. 13, we plot the emissivity used in this paper as well as the Lagache et al. (2004) ones for reference. The peak at $z \sim 1$ in our emissivities is due to the parameterization of the LF. Despite the shapes of the emissivities of Lagache et al. (2004) and ours are different, they display similar trends. The relative

wavelength	kind of galaxies	reference	$< z >$	b_{HOD}	b_{lin}
24	resolved	Magliocchetti et al. (2008)	0.79	1.70	
24	resolved	Magliocchetti et al. (2008)	2.02	6.17	
24	resolved	Brodwin et al. (2008)	2		3.1-5.3
24	resolved	Gilli et al. (2007)	0.75		1.3±0.1
24	resolved	Gilli et al. (2007)	0.8		1.4±0.1
24	resolved	Gilli et al. (2007)	1		1.8±0.2
100	resolved	Saunders et al. (1992)	0		0.86
160	background	Lagache et al. (2007)	1		2.4±0.2
250-350-500	background	Viero et al. (2009)	1.5	2.2±0.2	3±0.2
250	resolved	Cooray et al. (2010)	$2.1^{+0.4}_{-0.7}$	2.9±0.4	
350	resolved	Cooray et al. (2010)	$2.3^{+0.4}_{-0.7}$	3.2±0.5	
250	resolved	Cooray et al. (2010)	$2.6^{+0.3}_{-0.7}$	3.6±0.8	

Table 4. Linear and effective bias measurements. The third column gives the mean redshift of the galaxies probed and the last but one lists the HOD/effective bias values and the last one gives the linear bias.

contributions of high redshifts increases with wavelength while the contribution of low redshifts decreases. According to Jauzac et al. (2011), the model of Lagache et al. (2004) predicts too much power at high z. As the latter is forced to reproduce levels of the CIB and number counts, it does not predict enough power at low z. Therefore it predicts more galaxies at high z and less at low z. To illustrate how it influences our results, we show on Fig. 14 the ratios of the power spectra computed with our emissivities and those from Lagache et al. (2004). Up to 550 μm the ratio is around 1 up to $\ell \sim 10000$ and it increases strongly at higher ℓ. At longer wavelength, the difference is much larger. It is in line with the over-prediction of power at high redshift of the model of Lagache et al. (2004). The same halo parameters have been used for this plot, however it is clear that when fitting the model to the data with both emissivities we will not find the same halo parameters.

As said previously the Lagache et al. (2004) model predicts too much power at high z, thus we need to compare the contribution in redshift to the C_ℓ. They are given on Fig. 15. In both cases we observe the same trend : high redshift contribute more and more as the wavelength increases. However, with Lagache et al. (2004) emissivities this evolution goes faster. For instance, at 250 μm, the contribution of $1.5 < z < 3$ galaxies is of the same order of magnitude that those of $0.7 < z < 1.5$ whereas in our case the former is more than one order of magnitude inferior to the latter. As we go towards longer wavelengths, the two highest redshift bins have an increasing contribution, and both dominate the power spectrum at 850 μm using Lagache et al. (2004) emissivities whereas using our emissivities $0.7 < z < 1.5$ galaxies contribute also strongly. At 1.3 and 2 mm both the highest redshift bins contribute the most but in our case, only the highest redshift bin dominate and the $1.5 < z < 3$ bin has a smaller contribution. Therefore the shape of the emissivities strongly influences our results, parameters determination and redshift distribution. The interpretation of clustering measurements is thus based on the use of a reliable model of evolution of galaxies.

5.4. Contribution of LIRGs and ULIRGs

Star-forming galaxies are split in several categories according to their luminosities. Normal, luminous infrared, and ultra luminous infrared galaxies have luminosities $L_{IR} < 10^{11} M_\odot$, $10^{11} M_\odot < L_{IR} < 10^{12} M_\odot$, $L_{IR} > 10^{12} M_\odot$, respectively. LIRGs dominate the infrared energy output at $z \sim 1$ and ULIRGs at $z \sim 2$ (Pérez-González et al. 2005; Le Floc'h et al. 2005; Caputi et al. 2007) therefore we look at their contribution to the C_ℓ and to their evolution with the wavelength. To do so we split the emissivities in the following way :

$$\bar{j}_\lambda = \bar{j}_\lambda^{normal} + \bar{j}_\lambda^{LIRG} + \bar{j}_\lambda^{ULIRG} \tag{23}$$

and this contribution is squared in the C_ℓ. Therefore cross terms appear :

$$\begin{aligned} C_{\ell,total} &= C_{\ell,Normal} + C_{\ell,LIRG} + C_{\ell,ULIRG} + 2(\times C_{\ell,Normal/LIRG} \\ &+ 2C_{\ell,Normal/ULIRG} + C_{\ell,LIRG/ULIRG}) \end{aligned} \tag{24}$$

We plot in Fig. 16 the contributions of normal, LIRGs and ULIRGs. Note that the sum of the three contributions does not make the total power spectrum because the cross terms are not shown.

Normal galaxies and LIRGs both dominate the power spectrum up to 550 μm. The contribution of LIRGs increases slightly and finally dominates from 850 μm to 2 mm. ULIRGs never clearly dominate the power spectrum at long wavelength, however their relative contribution increases at long wavelengths, from 850 μm to 2 mm.

Therefore, we do recover what is expected from previous works. Normal galaxies dominate at low redshift, LIRGs at $z \sim 1$ and ULIRGs contribute in the same way as the others at high redshift and thus at long wavelengths.

6. Conclusion

We presented a new model of the clustering of star-forming galaxies in the Cosmic Infrared Background anisotropies. We interfaced a parametric model of star-forming galaxies evolution with a halo distribution approach. The model is fully parametric. Fixing the cosmology, it depends on the parameters of the model of galaxies and the HOD. We computed power spectra from 100 μm to 2 mm for IRAS, Spitzer/MIPS, Herschel/SPIRE and Planck/HFI spectral bands. We showed how power spectra can depend on the parameters and we concluded that the parameters of the model of galaxies can hardly be constrained using C_ℓ only. Number counts and luminosity functions data are required. Fixing them at the mean values found by Béthermin et al. (2011), we explored the HOD parameters constraints and degeneracies. The combination of C_ℓ and counts/LF data do not break the degeneracies but constraints are slightly improved. Some of the parameters are strongly degenerate, especially M_{min} and M_{sat} with $M_{sat} = xM_{min}$ with $x \sim 3$ where x is the direction of the degeneracy.

We have shown that the 1-halo term can be detected at all wavelengths and that galaxies at high redshift lie in smaller halos than

those at lower redshift. The level of the shot noise might not be reached with certain instruments such as Planck because of their angular resolution. However, this does not apply to the South Pole Telescope and to Herschel as they have a better angular resolution.

Using our fiducial model, we computed the halo mass and redshift contribution to the power spectra. Higher redshift galaxies contribute more at long wavelengths. Not surprisingly, the 1- and 2- halo terms do not have the same mass dependence. We found that high mass halos contribute the most to the 1 halo term whereas the 2-halo term is dominated by intermediate mass halos which are most numerous. Our model strongly depends on the emissivity given by the evolution model of galaxies, and we compare the resulting C_ℓs with those obtained using the emissivities coming from Lagache et al. (2004). We have shown that the halo parameters strongly depend on the emissivities when data are fitted.

In order to avoid the use of a model of evolution of galaxies, we have split the redshift range in four bins and computed the C_ℓ using the mean emissivity on these four redshift bins as in Amblard et al. (2011). We considered these four parameters as free. They are not very well constrained, they cannot give any constraints on models of galaxies.

We investigate the contribution of LIRGs and ULIRGs to the power spectra and its evolution with the wavelength. Our results are in agreement with previous studies of normal galaxies, LIRGs and ULIRGs contribution to the CIB and to the luminosity functions. Normal galaxies dominate the power spectrum at low redshift. As the redshift increases, LIRGs dominate C_ℓ. Meanwhile, the contribution of ULIRGs keeps increasing up to 2 mm.

The main unknown in CIB anisotropies power spectrum measurements are the redshift distributions of CIB galaxies. The coming results from Planck and Herschel will enable a great leap in the understanding of the clustering of star-forming galaxies and its redshift evolution, measuring the cross power spectra between wavelengths. These new measurements will help to break some degeneracies and will allow to make more precise measurements of the star formation density at high redshift, and the characteristic mass of the dark matter halo at which the efficiency of the star formation is maximal.

Acknowledgements. Part of the research described in this paper was carried out at the Jet Propulsion Laboratory, California Institute of Technology, under a contract with the National Aeronautics and Space Administration. The authors would like to thank Mathieu Langer for very useful comments that improved this manuscript.

References

Amblard A., Cooray A., Dec. 2007, ApJ, 670, 903
Amblard A., Cooray A., Serra P., et al., Jan. 2011, ArXiv e-prints
Austermann J.E., Dunlop J.S., Perera T.A., et al., Jan. 2010, MNRAS, 401, 160
Berta S., Magnelli B., Lutz D., et al., Jul. 2010, A&A, 518, L30+
Béthermin M., Dole H., Beelen A., Aussel H., Mar. 2010, A&A, 512, A78+
Béthermin M., Dole H., Lagache G., Le Borgne D., Penin A., May 2011, A&A, 529, A4+
Brodwin M., Dey A., Brown M.J.I., et al., Nov. 2008, ApJ, 687, L65
Caputi K.I., Dole H., Lagache G., Puget J., Apr. 2006, ArXiv Astrophysics e-prints
Caputi K.I., Lagache G., Yan L., et al., May 2007, ApJ, 660, 97
Cooray A., Sheth R., Dec. 2002, Phys. Rep., 372, 1
Cooray A., Amblard A., Wang L., et al., Jul. 2010, A&A, 518, L22+
Eisenstein D.J., Hu W., Mar. 1998, ApJ, 496, 605
Farrah D., Lonsdale C.J., Borys C., et al., Apr. 2006, ApJ, 641, L17
Fernandez-Conde N., Lagache G., Puget J.L., Dole H., Apr. 2008, A&A, 481, 885
Fixsen D.J., Dwek E., Mather J.C., Bennett C.L., Shafer R.A., Nov. 1998, ApJ, 508, 123
Fowler J.W., Atacama Cosmology Telescope Team, Jan. 2010, In: Bulletin of the American Astronomical Society, vol. 41 of Bulletin of the American Astronomical Society, 599–+
Gao L., White S.D.M., Jenkins A., Stoehr F., Springel V., Dec. 2004, MNRAS, 355, 819
Gilli R., Daddi E., Chary R., et al., Nov. 2007, A&A, 475, 83
Grossan B., Smoot G.F., Nov. 2007, A&A, 474, 731
Haiman Z., Knox L., Feb. 2000, ApJ, 530, 124
Hall N.R., Keisler R., Knox L., et al., Aug. 2010, ApJ, 718, 632
Jauzac M., Dole H., Le Floc'h E., et al., Jan. 2011, A&A, 525, A52+
Kennicutt R.C. Jr., May 1998, ApJ, 498, 541
Knox L., Cooray A., Eisenstein D., Haiman Z., Mar. 2001, ApJ, 550, 7
Lagache G., Abergel A., Boulanger F., Désert F.X., Puget J., Apr. 1999, A&A, 344, 322
Lagache G., Dole H., Puget J.L., Jan. 2003, MNRAS, 338, 555
Lagache G., Dole H., Puget J.L., et al., Sep. 2004, ApJS, 154, 112
Lagache G., Puget J., Dole H., Sep. 2005, ARA&A, 43, 727
Lagache G., Bavouzet N., Fernandez-Conde N., et al., Aug. 2007, ApJ, 665, L89
Larson D., Dunkley J., Hinshaw G., et al., Feb. 2011, ApJS, 192, 16
Le Floc'h E., Papovich C., Dole H., et al., Oct. 2005, ApJ, 632, 169
Magliocchetti M., Silva L., Lapi A., et al., Mar. 2007, MNRAS, 375, 1121
Magliocchetti M., Cirasuolo M., McLure R.J., et al., Jan. 2008, MNRAS, 383, 1131
Magliocchetti M., Santini P., Rodighiero G., et al., Jul. 2011, MNRAS, 1055–+
Navarro J.F., Frenk C.S., White S.D.M., May 1996, ApJ, 462, 563
Oliver S.J., Wang L., Smith A.J., et al., Jul. 2010, A&A, 518, L21+
Papovich C., Dole H., Egami E., et al., Sep. 2004, ApJS, 154, 70
Pénin A., Lagache G., Noriega-Crepo A., et al., May 2011, ArXiv e-prints
Pérez-González P.G., Rieke G.H., Egami E., et al., Sep. 2005, ApJ, 630, 82
Planck Collaboration, Ade P.A.R., Aghanim N., et al., Jan. 2011, ArXiv e-prints
Puget J., Abergel A., Bernard J., et al., Apr. 1996, A&A, 308, L5+
Saunders W., Rowan-Robinson M., Lawrence A., et al., Jan. 1990, MNRAS, 242, 318
Saunders W., Rowan-Robinson M., Lawrence A., Sep. 1992, MNRAS, 258, 134
Scott K.S., Yun M.S., Wilson G.W., et al., Jul. 2010, MNRAS, 405, 2260
Tinker J., Kravtsov A.V., Klypin A., et al., Dec. 2008, ApJ, 688, 709
Tinker J.L., Wetzel A.R., Aug. 2010, ApJ, 719, 88
Tinker J.L., Wechsler R.H., Zheng Z., Feb. 2009, ArXiv e-prints
Viero M.P., Ade P.A.R., Bock J.J., et al., Dec. 2009, ApJ, 707, 1766

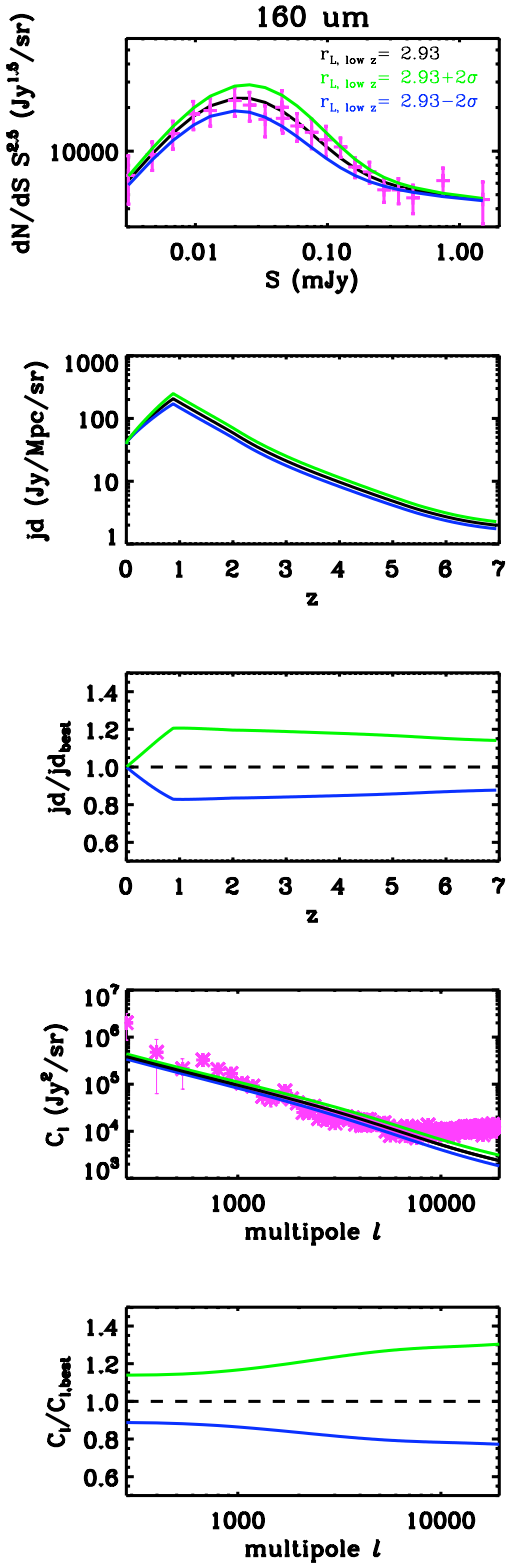

Fig. 6. Counts at 160 μm, emissivities and clustering power spectrum for three values of $r_{L_\star,lz}$, the best fit and the best fit $\pm 2\sigma$. Pink crosses are data, Béthermin et al. (2010) for the counts and Lagache et al. (2007) for the power spectrum. Top panel : differential number counts at 160 μm. 2nd panel : mean emissivities at 160 μm. 3rd panel : ratio of the modified emissivities compared to the best fit one at 160 μm. 4th panel : power spectra of the clustering at 160 μm. Bottom panel : ratio of the modified power spectra compared to the best fit one at 160 μm. A small change of $r_{L_\star,lz}$ leads to a 20 % modification on the emissivities and on 15-35% on the C_ℓ.

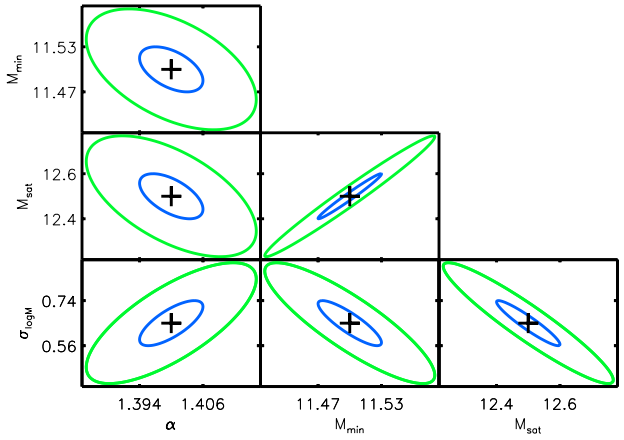

Fig. 8. 1σ (blue) and 2σ (green) likelihood contours of the halo model parameters computed with mock data from 100 μm to 1.3 mm.

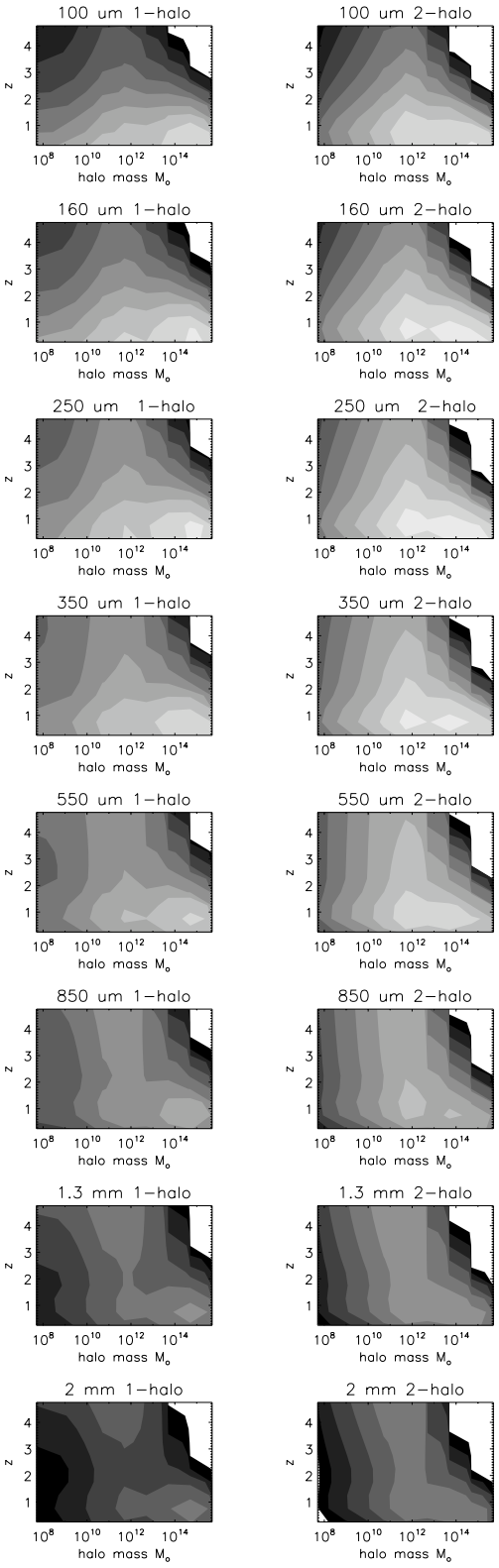

Fig. 10. Contribution of halo masses and redshift to the C_ℓ from 100 μm to 2 mm. The first column shows the redshift and mass contribution to the 1-halo term (ℓ = 2002) and the second column represents the same contributions to the 2-halo term (ℓ = 100). The light grey corresponds to the highest contribution to the C_ℓs. The step of the color range is logarithmic and the scale is the same for both columns. The 1-halo term is dominated by high masses at low z at all wavelength. At all wavelength, the 2-halo term is dominated by a large range of masses at low z and by intermediate masses at higher z. The 1- and 2-halo term are sensitive to different mass regimes. The former to high mass halos and the latter to intermediate mass halos.

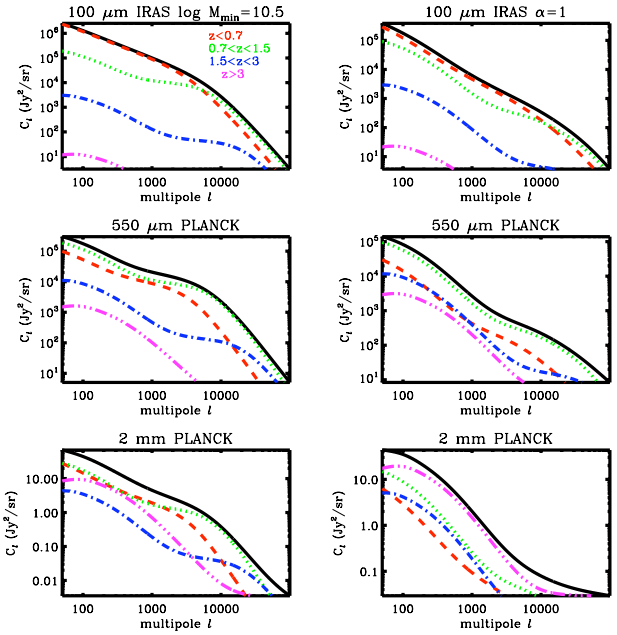

Fig. 11. Redshift distribution for several wavelengths for halo parameters different from the values of the fiducial model. The left panels are for $\log M_{min} = 10.5$ instead of $\log M_{min} = 11.5$ and the right panels are for $\alpha = 1$ instead of $\alpha_{sat} = 1.4$. The redshift distribution depends strongly on the chosen halo parameters although the same trend is observed : the low redshift dominate at short wavelengths, this contribution decreases with the wavelength and as the wavelength gets longer the contribution of high redshifts increases.

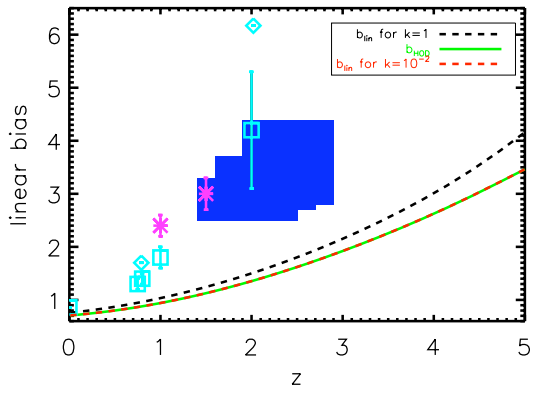

Fig. 12. Linear bias for several values of k (in (Mpc/h)$^{-1}$) and HOD bias. Light blue squares and diamonds bias values from resolved galaxies and pink crosses represent biases from unresolved galaxies measurements (see Table 4). The big blue squares represent the HOD biases coming from resolved galaxies from Cooray et al. (2010). Light blue diamonds and squares show HOD and linear biases, respectively.

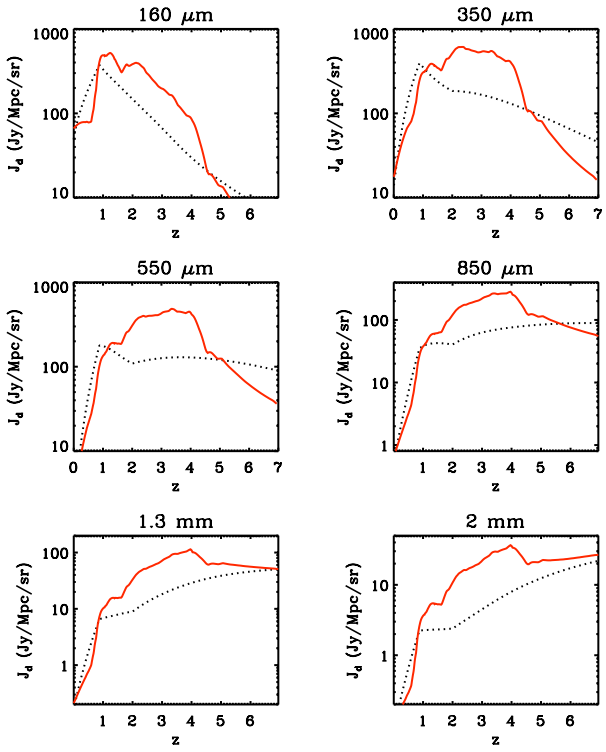

Fig. 13. Emissivities used by Viero et al. (2009) coming from Lagache et al. (2004) (red continous line) and ours (black dotted line) coming from Béthermin et al. (2011) at several wavelengths.

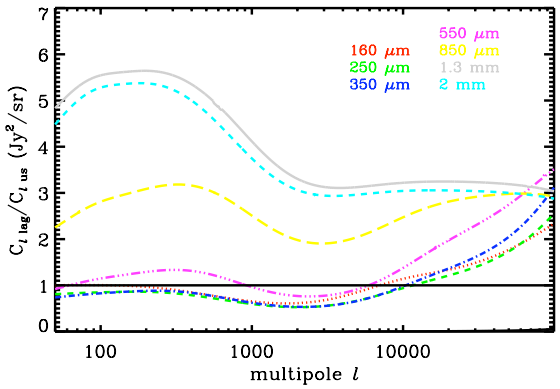

Fig. 14. Power spectra ratios computed using the emissivities of Lagache et al. (2004) ($C_{\ell,lag}$) and Béthermin et al. (2011) ($C_{\ell,us}$), for several wavelengths.